Title

Glioblastoma evolution and heterogeneity from a 3D whole-tumor perspective

Journal

Cell, 187(2)

ISSN

0092-8674

Authors

Mathur, Radhika
Wang, Qixuan
Schupp, Patrick G
et al.

Publication Date

2024

DOI

10.1016/j.cell.2023.12.013

Peer reviewed

Published in final edited form as:

Cell. 2024 January 18; 187(2): 446–463.e16. doi:10.1016/j.cell.2023.12.013.

Glioblastoma evolution and heterogeneity from a 3D whole-tumor perspective

Radhika Mathur[1], **Qixuan Wang**[2], **Patrick G. Schupp**[1], **Ana Nikolic**[3], **Stephanie Hilz**[1], **Chibo Hong**[1], **Nadia R. Grishanina**[1], **Darwin Kwok**[1], **Nicholas O. Stevers**[1], **Qiushi Jin**[2], **Mark W. Youngblood**[4], **Lena Ann Stasiak**[2], **Ye Hou**[2], **Juan Wang**[2], **Takafumi N. Yamaguchi**[5], **Marisa Lafontaine**[1], **Anny Shai**[1], **Ivan V. Smirnov**[1], **David A. Solomon**[6], **Susan M. Chang**[1], **Shawn L. Hervey-Jumper**[1], **Mitchel S. Berger**[1], **Janine M. Lupo**[1], **Hideho Okada**[1], **Joanna J. Phillips**[1], **Paul C. Boutros**[5], **Marco Gallo**[3,7], **Michael C. Oldham**[1], **Feng Yue**[2,*], **Joseph F. Costello**[1,*,↑]

[1]Department of Neurological Surgery, University of California San Francisco

[2]Department of Biochemistry and Molecular Genetics, Feinberg School of Medicine, Northwestern University

[3]Department of Biochemistry & Molecular Biology, University of Calgary

[4]Department of Neurological Surgery, Feinberg School of Medicine, Northwestern University

[5]Department of Human Genetics, University of California, Los Angeles

[6]Department of Pathology, University of California San Francisco

[7]Department of Pediatrics, Baylor College of Medicine, Texas Children's Hospital

Summary

Treatment failure in the lethal brain tumor glioblastoma (GBM) is attributed to intratumoral heterogeneity and tumor evolution. We utilized 3D surgical neuronavigation to acquire samples representing the whole tumor from patients mapped by 3D spatial coordinates. Integrative tissue and single-cell analysis revealed sources of genomic, epigenomic, and microenvironmental intratumoral heterogeneity and their spatial patterning. By distinguishing tumor-wide molecular features from those with regional specificity, we inferred GBM evolutionary trajectories from neurodevelopmental lineage origins and initiating events such as chromothripsis to emergence of genetic subclones and spatially-restricted activation of differential tumor and microenvironmental programs in the core, periphery, and contrast enhancing regions. Our work depicts GBM evolution and heterogeneity from a 3D whole-tumor perspective, highlights potential therapeutic targets that might circumvent heterogeneity-related failures, and establishes an interactive platform enabling

[↑]Lead contact (Joseph.Costello@ucsf.edu).

[*]Senior author

Author contributions

R.M. and J.F.C. conceptualized this project with input from F.Y., M.C.O., M.G., H.O., P.C.B., and S.M.C. Surgical samples were collected by S.L.H., M.S.B., and A.S. Experiments were designed and performed by R.M., N.G., N.O.S., C.H., A.N., Q.J., M.Y., L.A.S., and Y.H. Genomic data were analyzed by R.M., Q.W., P.G.S., A.N., D.K., T.Y., J.W., D.A.S. and I.S. Imaging data were analyzed by M.L., S.H., and J.L. Histopathological analysis was conducted by J.J.P. The manuscript was written by R.M. with all authors contributing to review and editing.

Declaration of interests

The authors declare no competing interests.

360° visualization and analysis of 3D spatial patterns for user-selected genes, programs, and other features across whole GBM tumors.

Graphical Abstract

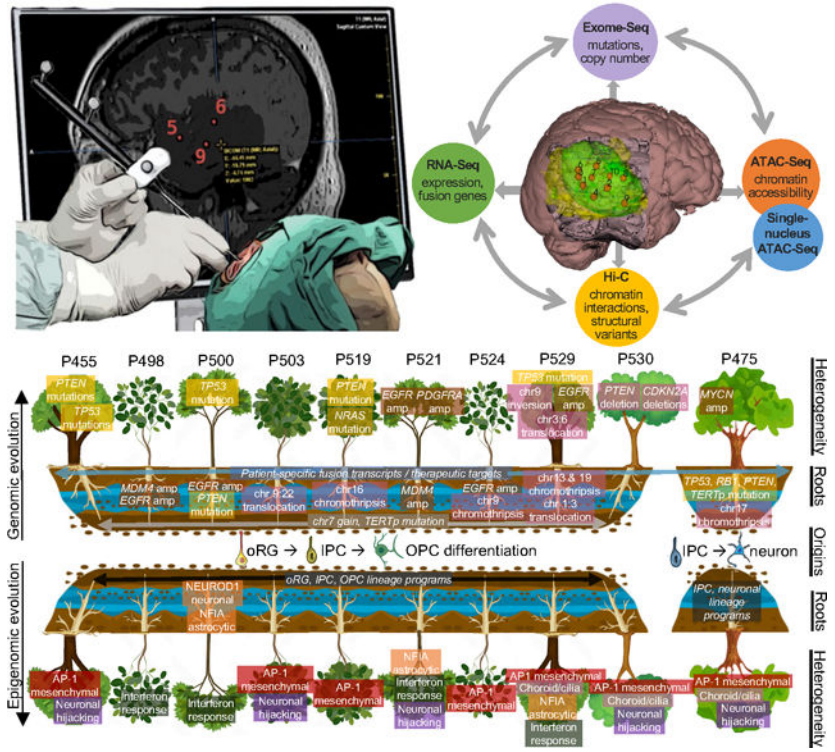

Introduction

Pathologists have long observed intratumoral heterogeneity in glioblastoma (GBM), coining the original name “glioblastoma multiforme” to reflect the diverse cellular forms they observed. Treatment failure in GBM is often attributed to intratumoral heterogeneity as it provides diversity upon which selection can act to foster outgrowth of treatment-resistant clones[1–3]. Intratumoral heterogeneity can occur in many forms – from mutations and structural variants to differences in chromatin landscapes and transcriptional regulation. Intratumoral heterogeneity also encompasses nonmalignant cells in the tumor microenvironment including neuronal, glial, and immune populations that may functionally interact with malignant cells and contribute to tumor evolution. The extent of intratumoral heterogeneity in GBM and nearly all solid tumors remains unknown as most studies, including those led by The Cancer Genome Atlas (TCGA)[4–7], rely on evaluation of single tissue biopsies per patient. Intratumoral heterogeneity poses major challenges to interpretation of these studies as determinations of mutational frequency, transcriptional state, etc. are dependent upon the region sampled and unlikely to be representative of the whole tumor. For example, GBM molecular subtypes initially proposed for interpatient classification and personalized medicine[6] were later found to differ amongst samples from the same tumor[8,9] and to reflect transcriptional output not only of malignant cells, but also of

nonmalignant cells admixed in tissue biopsies[10]. While single-cell and spatial transcriptomic technologies distinguish malignant cells from microenvironmental cell types, they are also typically based on single tissue biopsies and lack context within the whole tumor. As sparse sequencing reads are obtained from individual cells, cells are typically grouped and assigned to 'states'[11–15]. Intratumoral heterogeneity and capacity for evolution are evident as cells from the same tumor are present in different states and show 'plasticity' or the ability to transition between states[12,16,17]. Much remains to be learned of these states including their molecular drivers, the extent to which they are heterogeneous across whole tumors, and mechanistic underpinnings of plasticity. Moreover, despite decades of analyses, the truncal genetic events for each tumor are not defined beyond those commonly shared across patients and much is unknown regarding macro-scale patterns of epigenomic programs and microenvironments across whole tumors.

To directly characterize intratumoral heterogeneity in whole GBM tumors, we collaborated with neurosurgeons and a multi-disciplinary clinical team to design a novel 3D spatial sampling approach. For 10 patients with newly diagnosed, treatment-naïve IDH-wildtype (WT) GBM (CNS WHO grade 4), we utilized 3D surgical neuronavigation to safely acquire 103 spatially mapped samples representing maximal tumor diversity each mapped by 3D spatial coordinates. We integrated these coordinates with pre-operative MRI scans to generate 3D models enabling 360° visualization of sample locations in context of the brain and whole tumor, distinguishing contrast-enhancing (CE) regions (Fig 1A, Table S1). We interrogated samples with a complementary and cross-validating set of genomic and epigenomic sequencing assays applied to tissue and/or single cells. Integrative analysis provided a 3D-spatially resolved view of GBM heterogeneity, redefining current understanding and unveiling insights into its earliest origins, evolution, and vulnerabilities. Our 3D spatial map of GBM is publicly accessible on an interactive online platform (https://3d-gbms.shinyapps.io/search/) that enables 360° visualization of user-selected features, enabling interrogation of their intratumoral heterogeneity and selection of pan-tumor targets that may avoid heterogeneity-related treatment failures.

Results

3D spatial sampling reveals patterns of GBM infiltration and clonal expansion

The infiltrative nature of GBM poses surgical challenges as malignant cells beyond resection margins give rise to recurrences. To examine the spatial distribution of malignant cells within whole tumors, we utilized WES-derived copy number data to quantify the proportion of malignant cells in each sample ("purity" or ψ). Sample purity spanned a full range (mean ψ=0.63, range 0–0.985). Although surgical resection sometimes focuses within borders of CE regions, we found no significant difference in purity between samples from CE and non-CE regions (Fig 1B). Malignant cells are thus extensively infiltrated beyond CE regions, providing a molecular basis for additional survival benefit from maximal resection of CE and non-CE regions[18,19]. We examined whether distribution of malignant cells followed a radial growth model but found no relationship between purity and relative distance (d) of each sample between the MRI-defined tumor centroid (0) and periphery (1) (Fig 1C). We also calculated inter-sample distances and found that purity differences were only

modestly associated with distance between samples (Fig S1A, Table S2). Thus, malignant and nonmalignant cells are intermixed throughout GBM tumors from centroid to periphery. Some samples were located at or beyond the periphery and had low purity, but detectable oncogene amplifications revealing malignant cell infiltration into the surrounding brain (Fig 1D, Fig S1B). Some samples from CE regions in the tumor core also had low purity and contained regions of necrosis (Fig 1D, Fig S1C).

Whole-tumor sampling enables inference of evolutionary trajectories as genomic alterations and programs detected tumor-wide represent cell-of-origin or the initial clonal expansion while those with intratumoral heterogeneity represent later events (Fig 1E). We constructed phylogenetic trees that distinguished truncal mutations from branch mutations present in only one or a subset of samples and grouped mutations from each patient into putative clonal clusters[20] (Fig S1D–E, Table S3). In several patients, multiple clonal expansions occurred concurrently resulting in formation of genetic subclones. Samples from P530 split into two genetic subclones located in distinct masses in the left temporal and frontal regions of the brain (Fig 1F, Fig S1F–G). P530 samples from the same subclone were 2.8cm apart on average while samples from different subclones were 8.4cm apart. While samples from P529 also split into two genetic subclones, they were spatially intermixed with samples from the same subclone no more physically close (average 1.8cm) than samples from different subclones (average 1.6cm) (Fig 1G–H, Fig S1H). Our 3D spatial approach thus allows us to estimate physical sizes of genetic subclones and their relative orientations within whole tumors. We find that clonal expansions in GBM occur in divergent manners – from independent, spatially-restricted outgrowth into distant brain regions to concurrent growth and infiltration of subclones into each other in the same region.

Oncogene amplification and tumor suppressor deletion on the whole-tumor scale

Oncogene amplifications are major drivers in GBM and occur principally on extrachromosomal (ec) DNA on which regulatory elements are retained[21–25]. We detected oncogene amplifications by high copy-number (Fig 2A, Fig S2A) and high levels of accessible chromatin and physical chromatin interactions with preserved underlying structures (Fig 2B–C, Fig S2B). *MDM4* amplifications were detected tumor-wide in two patients indicating they likely occurred early in tumor evolution (Fig 2A). The *MDM4*-amplified region in P498 had breakpoints within *OPTC* and *NFASC* (Fig 2B) and gave rise to *NFASC*::*OPTC* fusion transcripts present tumor-wide (Fig 2D). *EGFR* was amplified in five patients with two showing intratumoral heterogeneity. In P529, *EGFR* was amplified only in subclone-*B* (Fig 1G) indicating it was not involved in early tumorigenesis but co-occurred with *TP53* mutation to drive subclonal outgrowth. In P521, *EGFR* amplification was high in the tumor region containing samples 1–4 while amplification of another oncogenic tyrosine kinase *PDGFRA* was high in the tumor region containing samples 6–8 (Fig 2E, S2C). *MYCN* was amplified in P475 and showed intratumoral heterogeneity. *MYCN* amplification is frequent in the variant of IDH-WT GBM with primitive neuronal component[26,27], histological features of which were identified in this patient (Fig S2D). However, this amplification was not detected in the diagnostic biopsy sample analyzed by our clinical NGS panel, highlighting limitations of single tissue biopsies for clinical diagnostics in the context of GBM intratumoral heterogeneity.

Tumor suppressor deletions are also critical GBM driver events. *PTEN* showed focal deletion only in P530 samples from the temporal region (Fig 2F, S2E). Interestingly, *de novo* loop formation across deletion breakpoints caused enhancer-hijacking resulting in upregulation of *FAM35A* and *RNLS* in the temporal region (Fig 2G–H). While *CDKN2A* underwent homozygous deletion across the whole P530 tumor, the deletion in the temporal region was larger (~690kbp) than the frontal region (~395kbp) (Fig 2I–J). While the larger deletion in the temporal region caused loss of *MTAP, de novo* loop formation across deletion breakpoints caused enhancer-hijacking and upregulation of *KLHL9* (Fig 2K). Tumor suppressor deletion thus reshapes both the GBM genome and epigenome and can occur independently and concurrently in different regions of the same tumor, manifesting in multiple forms of intratumoral heterogeneity.

Structural variants disrupt the genome and epigenome to drive GBM evolution

As structural variants (SVs) induce *de novo* chromatin interactions, we utilized Hi-C datasets to systematically identify SVs[28–30] (Table S4). We identified five cases of chromothripsis[31,32] spanning ~3–60Mb where SVs clustered closely together. In P524, chromothripsis occurred at the *CDKN2A* locus indicating it was responsible for deletion of this tumor suppressor. Chromothripsis created fusion genes including *SLC24A2*::*MLLT3* and *TESK1*::*TRMT10B* which were in-frame and present in all samples except one with low purity (P524_1, ψ=0.04) (Fig 3A–B). In P529, chromothripsis occurred on chr13 and on chr19 (Fig 3C). The chr13 event was centered on the *RB1* tumor suppressor and created out-of-frame *RB1*::*LINC00441* fusion transcripts while the chr19 event fused *TTYH1*, which is recurrently involved in fusions driving embryonal brain tumors[33], with *FOSB,* a component of the AP-1 transcription factor. Both fusion transcripts were expressed in all P529 samples. Chromothripsis in P475 (chr17) and P519 (chr16) also created fusion transcripts present tumor-wide (Fig S3A). Thus, chromothripsis is one of the earliest driver events in GBM evolution. Despite their tumor-wide presence and impact on clinically important genes, no chromothripsis events were discovered by our clinical NGS panel presumably due to breakpoints in introns.

Other SVs showed intratumoral heterogeneity indicating they occurred later in tumor evolution or represented one of multiple early, contemporaneously evolving clonal expansions. In P529, *CDK2NA* was the breakpoint of a 110Mb inversion that spanned 78% of chr9 (Fig 3D–E). The inversion and resulting *TSC1*::*CDKN2B-AS1* fusion were detected only in subclone-*A* and were likely selected due to simultaneous inactivation of *CDKN2A* and *TSC1,* another glioma tumor suppressor[34]. Translocations were visible on Hi-C contact maps as aberrant inter-chromosomal interactions. In P529, a chr1:3 translocation creating an *EPS15*::*CRYBG3* fusion was present tumor-wide while a chr3:6 translocation creating a *LACE1*::*TIGIT* fusion was present only in subclone-*A* (Fig 3F, S3B–C). Thus, two chromothripsis events and the chr1:3 translocation occurred early in evolution of this tumor while the chr9 inversion and chr3:6 translocation occurred specifically in the subclone lacking *TP53* mutation and *EGFR* amplification (Fig 3G). The degree of heterogeneity between these subclones is remarkable given their spatial intermixing and cautions against extrapolation from individual samples to the whole tumor. We also identified translocations in other patients including one specific to the frontal region of P530 (Fig S3D–E). SVs thus

disrupt the genome and epigenome at multiple stages of GBM evolution, driving either early tumorigenesis or subclonal outgrowth and intratumoral heterogeneity.

GBM structural variants create fusion transcripts and precision therapeutic opportunities

As SV-induced fusion genes are specific to malignant cells, they provide opportunities for therapeutic intervention[35,36]. We identified an in-frame translocation-induced *BCR*::*NTRK2* fusion can be targeted by FDA-approved kinase inhibitors larotrectinib or entrectinib (Fig 3H). This fusion represented a tumor-wide vulnerability and therapeutic opportunity but was unfortunately missed by our clinical NGS panel due to breakpoints outside exons. The only fusion recurrently identified in our cohort *EGFR*::*SEPT14*[35] was subclonal in each case, limiting its therapeutic potential (Fig 3I, Table S4). From an immunotherapeutic perspective, fusion-derived peptides or mRNA may serve as neoantigens for personalized vaccines[37,38]. To explore this potential, we identified each patient's MHC variants and applied two algorithms to predict MHC-specific binding[39,40]. Fusions from each patient including validated tumor-wide fusions *EPS15*::*CRYBG3*, *RB1*::*LINC00441* and *TTYH1*::*FOSB* from P529 were predicted to generate peptides presented by MHC-I (Fig 3J, Fig S3F). These findings suggest unrealized clinical value of searching for tumor-wide fusion transcripts in patients upon diagnosis as they help identify clinically important SVs and present therapeutic opportunities ranging from targeted inhibition of fusion oncoproteins to potential neoantigens for precision immunotherapies.

Transcriptomic heterogeneity in 3D spatially-defined GBM microenvironments

We sought to investigate the full diversity and spatial relationships of GBM transcriptomic programs in their native context within whole tumors. We first analyzed gene expression profiles of spatially mapped samples in context of the original molecular subtypes defined using the TCGA-GBM cohort[6] (Fig 4A, Video S1). Although these subtypes were initially proposed for interpatient classification, only one patient (P500) showed consistent enrichment of the same subtype across samples. Samples classified as Proneural and Classical had high purity while samples classified as Mesenchymal and Neural had mixed and low purity respectively (Fig 4B). Neural and Proneural samples were located close to the periphery while Classical and Mesenchymal samples were located closer to the tumor core. The low-purity sample located outside the periphery P521_5 (ψ=0.03) was classified as Neural, consistent with this subtype primarily representing transcriptional programs of normal cell types present in the brain[10]. Individual genes defining each subtype showed variable expression across samples (Fig S4A) indicating these subtypes consisted of amalgamations of genes from diverse transcriptional programs and/or cell types that could be activated separately or in conjunction with each other.

To more precisely define GBM transcriptomic programs, we performed unsupervised covariation analysis as described previously in human brain tissues[41]. Using RNA-Seq data from spatially mapped samples, we derived modules (*R*_) each consisting of a unique set of co-expressed genes (Fig 4C, Table S5). We annotated modules by enrichment analysis and calculated correlations between average module expression and sample purity (R_ψ) and relative sample distance between centroid and periphery (R_d). Modules represented both tumor and microenvironmental programs, collectively capturing extensive

transcriptomic heterogeneity. Programs corresponding to oligodendrocytes (*R_brown*, R_ψ −0.82), astrocytes (*R_plum,* R_ψ −0.51), and neurons (*R_orangered3,* R_ψ −0.48) were expressed in low-purity Neural samples (Fig 4D). Their relative expression varied revealing some such as P503_2 (ψ=0.03) contained mainly astrocytes and oligodendrocytes while others such as P503_1 (ψ=0.00) also contained neurons (Fig 4C, S4B). Modules with strong spatial preference towards the tumor periphery (*R_lightcoral* R_d +0.44, *R_darkseagreen4* +0.40, and *R_pink* +0.39) were enriched for neuronal signatures and were expressed in neuron-containing samples such as P503_1, but also in Proneural samples containing almost exclusively tumor cells such as P530_6 (ψ=0.97) (Fig 4E, Fig S4C). These modules represent tumor cell-hijacking of neuronal programs as described in context of glioma-neuron synaptic communication and formation of neurite-like tumor microtubes[42–44]. The top-ranked gene in *R_darkseagreen4 FRRS1L* is critical for biogenesis and function of AMPA receptors[45,46], which are implicated in electrochemical communication at neuron-glioma synapses[42,44]. Other *R_darkseagreen4* genes including neuroligin *NLGN2* and neurexins *NRXN1, NRXN2,* and *NRXN3* also have roles in synapse formation (Fig S4D). *RUSC1,* the top-ranked gene for *R_lightcoral,* encodes a signaling adaptor that promotes neurite outgrowth[47] and may contribute to formation of neurite-like tumor microtubes. We thus reveal that neuronal hijacking occurs specifically at the GBM periphery and delineate specific hijacked genes including novel potential contributors to glioma-neuron communication and microtube formation for further investigation.

Whole-tumor transcriptomic analysis revealed programs active in GBM immune microenvironments. *R_blue* was strongly enriched for signatures of microglia (Fig 4C), the primary innate immune cells of the brain[48], containing canonical markers *AIF1* (Iba1) and *TMEM119.* We also identified modules corresponding to immunologically “hot” and “cold” microenvironments: *R_greenyellow* contained interferon signaling and T cell markers (Fig S4E) while *R_midnightblue* contained canonical markers of immunosuppressive alternately activated ‘M2’ macrophages *CD163*, *IL10*, and *MSR1.* Both were enriched towards the tumor core (R_d = −0.30 and −0.29 respectively). Samples with high *R_greenyellow* expression such as P521_2 were infiltrated by $Iba1^+$ microglia and $CD3^+$ T cells while samples with high *R_midnightblue* expression such as P529_9 were infiltrated by immunosuppressive $Iba^+/CD163^+$ microglia (Fig 4F). Analysis of GBM single-cell RNA-Seq data[49] confirmed *R_greenyellow* expression in T cells and *R_midnightblue* expression in myeloid cells (Fig S4F). Importantly, these modules reveal known and many novel potential contributors to GBM immune activation and to creation of the immunosuppressive environment to which immunotherapy failure is attributed. *R_greenyellow* includes PD-1 receptor *PDCD1*, PD-1 ligand *PDCD1LG2,* and butyrophilin genes which elicit T cell activation and are proposed immunotherapy targets[50]. *R_midnightblue* includes *S100A4,* which promotes immunosuppression and is a proposed glioma immunotherapy target[49], *SIGLEC7/9,* which is implicated in tumor evasion of immune surveillance[51], and *LRRC25,* which inhibits IFN and NF-kB signaling[52,53] but has yet to be investigated in cancer.

Mesenchymal differentiation in GBM is associated with increased aggressiveness, but debate continues on whether the signature is intrinsically captured in malignant cells or is a byproduct of the immune microenvironment[54]. *R_midnightblue* was enriched for the original Mesenchymal signature from bulk RNA-Seq[6] (Fig 4C)

indicating immunosuppressive microglia were present in regions undergoing mesenchymal differentiation and contributed to overall transcriptional output. *R_midnightblue* genes included *OSM*, which mediates immune cell-induction of mesenchymal GBM states[55]. Three other modules were also preferentially expressed in Mesenchymal samples (Fig 4G). *R_plum2* was enriched for tumor cell-intrinsic injury response/MES1 signatures[12,14] (Fig S4G) and was preferentially expressed towards the core (R_d = −0.23) including in spatially distant cores of P530 temporal and frontal regions (Fig 4H). *R_plum2* genes including *SAA1,* a clinical indicator of inflammation, and *SOD2,* a constituent of apoptotic signaling and oxidative stress, were highly expressed in necrosis-containing sample P529_7 located close to the core. *R_plum3* was enriched for the tumor cell-intrinsic MES2 signature[12] and included markers of GBM hypoxia response and glycolysis as well as pro-angiogenic factor *VEGFA* (Fig S4H). *R_plum3* was negatively correlated with *R_blue* (−0.45), indicating expression in regions depleted of microglia (Fig S4I). *R_darkred* contained genes involved in extracellular matrix organization and markers of GBM cancer-associated fibroblasts[57] (Fig S4H) including proposed therapeutic target *COL1A1*[56]. *R_darkred* was significantly enriched in CE regions (Fig 4I) including in multivariable analysis controlling for purity and relative distance from centroid ($p<5.9 \times 10^{-8}$). Thus, transcriptomic programs with different cellular origins and spatial proclivities collectively contribute to GBM mesenchymal differentiation.

To study regulatory mechanisms underlying transcriptomic programs, we conducted motif analysis on promoter and enhancer ATAC-Seq peaks linked to genes from each module (Table S5). PU.1 was most enriched for *R_blue*, consistent with its role in the myeloid lineage[58], while interferon-sensitive response element (ISRE) was most enriched for *R_greenyellow*. Remarkably, AP-1 was most enriched for *R_midnightblue, R_plum2, R_plum3,* and *R_darkred*. AP-1 is thus a critical mediator of multiple aspects of GBM mesenchymal differentiation including creation of an immunosuppressive microenvironment, tumor cell responses to injury and hypoxia, and physical reshaping of the extracellular matrix (Fig 4J).

Neurodevelopmental programs reflect GBM origins and contribute to heterogeneity

Transcriptomic analysis identified neurodevelopmental programs active tumor-wide that provided insight into GBM lineage origins. *R_turquoise* was strongly correlated with sample purity (R_ψ = +0.82) indicating expression in malignant cells across all patients in our cohort (Fig 5A). It was also the module most strongly correlated with purity across 136 primary IDH-WT GBM patients in the TCGA cohort[5,6](Fig S5A). *R_turquoise* was enriched for the signature of dividing intermediate progenitor (IPC) cells from the developing brain[59] (Fig 4C). Top-ranked genes included mitotic kinesin and checkpoint proteins – *KIF18A, KIF14, TTK, SKA1,* and *BUB1*– all of which are also expressed in dividing IPC cells[59] (Fig 5A). The dividing IPC program thus drives unchecked proliferation in GBM. Of note, *KIF18A* is implicated as a vulnerability in chromosomally unstable cancers and targeted inhibitors have been tested *in vivo*[60,61]. As *KIF18A* and other *R_turquoise* genes are expressed tumor-wide, they represent viable opportunities for therapeutic targeting with minimal risk of heterogeneity-related failures.

Outer-radial glia (oRG) are neural stem cells in the outer subventricular zone that produce either oligodendrocyte precursor cells (OPCs) or neurons through distinct transit-amplifying IPCs[62,63] (Fig 5B). *R_brown2* and *R_maroon* were enriched for oRG and OPC signatures respectively. *PTPRZ1,* which is expressed through oRG differentiation to OPCs[63], was a top-ranked gene (#5) in *R_maroon* along with its ligand *PTN* (#12). *PTPRZ1, PTN,* and other *R_maroon* genes were robustly expressed and in the open 'A' chromatin compartment in high-purity samples such as P524_9 (ψ=0.89) but were silenced and in the closed 'B' compartment in low-purity samples such as P524_1 (ψ=0.04) (Fig S5B). Given the importance of chromatin architecture in differentiation[64], these findings are consistent with GBM originating along the lineage trajectory of oRG differentiation to OPCs. oRG-like populations exhibiting *PTPRZ1*-mediated mitotic somal translocation have been described in human GBMs[65] and *PTPRZ1* is a proposed therapeutic target[66,67] for which our results provide tumor-wide support.

Notably, *R_brown2* and *R_maroon* expression were low in all samples from P475, the GBM with primitive neuronal component (Fig 5C). This GBM variant has yet to be characterized at the transcriptional level and little is known of the molecular basis underlying its distinct histological features. We identified *R_ivory* as specific to P475 and highly correlated with purity indicating activation across tumor cells ($R_{\psi P475}$ = +0.93, Fig 5C). *R_ivory* genes included *NKX2–1* (which encodes the TTF-1 marker specific to this GBM variant[27]), a network of transcription factors key for neuronal fate specification including *NEUROG2* and *NEUROD4* (Fig 5D), as well as markers of IPC differentiation to neurons such as *PPP1R17 and NHLH2*[68]. Taken together with specific absence of oRG and OPC signatures, these findings implicate origin in distinct neurodevelopmental lineages as a molecular basis of differences observed in this GBM variant. To assess generalizability of these findings, we analyzed a high-purity sample (ψ=0.97) from a second patient diagnosed with this GBM variant (P565) and found robust expression of *R_ivory* and absence of *R_brown* and *R_maroon* (Fig S5C). Immunostaining confirmed presence of TTF-1 and absence of PTPRZ1 protein in both P475 and P565 (Fig 5E). Our whole-tumor transcriptome analysis thus elucidates neurodevelopmental lineage origins of GBMs including a divergent lineage that gives rise to the GBM variant with primitive neuronal component.

Unexpectedly, transcriptomic analysis identified a program *R_red* that was enriched for choroid plexus and ependymal signatures. Many of its 376 constituent genes encoded components of motile cilia (Fig S5D), which are present on ependymal cells that line the choroid plexus and function in circulation of cerebrospinal fluid. Promoters and enhancers linked to *R_red* genes were enriched for the binding motif of RFX transcription factors ($p<1 \times 10^{-61}$) (Table S5) which control ciliogenesis in ependymal cells[69]. We considered the possibility that samples with high expression of *R_red* contained choroid plexus tissue but found no evidence by histology. These samples were spatially distant from brain ventricles (Fig S5E) and tended to be high purity (R_{ψ} = +0.34) indicating this program was aberrantly expressed in malignant cells. *R_red* expression was also restricted to specific genetic subclones such as subclone-*A* in P529 (Fig 3G) and frontal samples in P530. Thus, malignant GBM cells may aberrantly activate RFX-mediated expression of choroid/cilia programs in the course of tumor evolution.

As programs reflecting cell lineage and transcription factor activity are encoded in chromatin, we sought to directly characterize chromatin landscapes across whole GBM tumors. We applied unsupervised covariation analysis to ATAC-Seq data from the same samples focusing on the 20% most variable peaks (*A_)* as well as the subset of peaks we characterized as promoters or enhancers linked to one or more genes (*L_)* (Fig 5F, S5F). We defined modules consisting of up to several thousand co-accessible peaks, collectively capturing inter- and intratumoral heterogeneity in GBM chromatin landscapes (Fig 5G, Table S6). These chromatin analyses reinforced and extended findings from transcriptome analysis regarding neurodevelopmental lineage origins of GBM. ATAC signal at *L_navajowhite1* peaks was strongly correlated with purity except in P475, the GBM with primitive neuronal component (Fig 5H). This module contained 1,364 peaks of which 70 were linked to *PTPRZ1* and 23 to *LHFPL3,* the top-ranked gene in the *R_maroon* OPC module. P475-specific modules *A_thistle* and *A_plum* showed strong motif enrichment for NEUROD1 (Fig 5G), a pioneer transcription factor for neuronal fate commitment that binds to and activates target genes even in their closed heterochromatin states[70]. NEUROD1 activation is consistent with broader activation of neuronal fate specification programs in GBM with primitive neuronal component (Fig 5D). Interestingly, the P500-specific module *A_darkseagreen3* was also strongly enriched for the NEUROD1 motif (Fig 5G). *A_darkseagreen3* included peaks at the *NEUROD1* promoter and an intronic *NEUROD1* enhancer, each containing NEUROD1 footprints, indicating an auto-regulatory loop (Fig 5I, Fig S5G). *NEUROD1* was highly expressed in P500 as well as in P475 and P565 (Fig 5J). Thus, while NEUROD1 activation in GBM with primitive neuronal component reflects lineage origins, NEUROD1 can also become aberrantly active in GBM and contribute to heterogeneity (Fig 5K).

Intratumoral heterogeneity of GBM chromatin landscapes at single-cell resolution

We next sought to investigate sources of intratumoral heterogeneity in GBM chromatin landscapes. To distinguish microenvironmental from tumor cell programs, we generated single-nucleus ATAC-Seq (snATAC) data for 10 spatially mapped samples from 4 of the patients in our study – a total of 30,498 cells (Fig 6A, Table S7). Cells grouped by sample and neoplastic status on UMAP projections with non-neoplastic cells forming multiple groups representing distinct microenvironmental cell types (Fig 6B, S6A–C). We identified modules corresponding to oligodendrocytes, neurons, and microglia and found that differences in cell type composition between samples were readily inferred by differences in ATAC signal at module constituent peaks (Fig 6C, S6D). As with transcriptome analysis, modules most negatively correlated with sample purity represented oligodendrocytes (*A_lavenderblush2,* $R_\psi = -0.54$, *L_coral,* $R_\psi = -0.68$) (Fig 5C). While peaks from these modules were accessible only in mature oligodendrocytes from normal adult brains[71], those from *A_coral* were also accessible in OPCs (Fig 6D). *A_coral* included 8 enhancers of *SOX10,* which has critical roles in oligodendrocyte lineage specification and terminal differentiation[72] (Fig S6E). SOX motifs were most enriched amongst constituent peaks of *A_coral* as well as of *A_lavenderblush2* and *L_coral* (Fig 5G). Whole-tumor chromatin analysis thus reveals in situ epigenomic programs and regulatory machinery of microenvironmental cells present in GBM tumors. While single-cell data alone is limited in defining chromatin landscapes due to variability introduced during cell dissociation and

sparse reads from individual cells, our combination of tissue and single-cell approaches, cross-referenced with gene expression, establishes open chromatin landscapes of cell types as they are in intact tumors at the resolution of individual gene regulatory elements.

Analysis of GBM chromatin landscapes further elucidated intratumoral heterogeneity of tumor programs. We identified striking intratumoral heterogeneity between P521 samples with high *EGFR* versus *PDGFRA* amplification (Fig 2E, 5G). Single-cell analysis revealed that these amplifications were mutually exclusive amongst neoplastic cells (Fig 6E). *EGFR*-amplified cells showed activation of *A_plum3*, a program normally active in astrocytes, while *PDGFRA*-amplified cells showed activation of *A_yellowgreen and A_coral,* programs normally active in OPCs (Fig 6D, 6F). Thus, *EGFR* and *PDGFRA*-amplified cells differentiated along diverse glial sub-lineages, creating heterogeneity evident both at 3D-spatial and single-cell resolution. *A_plum3* peaks were strongly enriched for the Nuclear Factor 1 motif (Fig 5G). Nuclear Factor 1A (NFIA) forms a complex with SOX9 to orchestrate astrocyte-specific gene expression while directly antagonizing SOX10 induction of oligodendrocyte-specific genes[73,74]. *A_plum3* included clusters of peaks at *SOX9* and at astrocyte-specific genes including *ADCY2* and *ADCYAP1R1* (Fig S6F). *SOX9* was highly expressed in *EGFR*-amplified samples while *SOX10* was highly expressed in *PDGFRA*-amplified samples (Fig S6G). Taken together, these results reveal that NFIA altered chromatin landscapes to specify *EGFR*-amplified cells to the astrocytic fate while *PDGFRA*-amplified cells differentiated towards the oligodendroglial fate (Fig 6G). As astrocyte (AC)-like and OPC-like GBM cell states have been identified by single-cell RNA-Seq[12], we examined the relationship between these cell states and the chromatin programs we defined. Genes linked to *A_plum3* and other NFIA-enriched modules were highly expressed in the AC-like state while genes linked to *A_yellowgreen* and *A_coral* were expressed in the OPC-like state (Fig S6H). Thus, we define open chromatin landscapes of different GBM cell states and reveal their 3D spatial distributions within whole tumors. Further, we implicate NFIA/SOX9 and SOX10 as potential mediators of transitions between the AC-like and OPC-like cell states.

We next investigated whether any chromatin programs were consistently associated with genomic alterations across patients. *L_salmon4* was associated with *EGFR*-amplification at the sample-level (Fig 6H) and at the single-cell level for patients with intratumoral heterogeneity (Fig 6I). *L_salmon4* included five peaks linked to *ELOVL2,* which supports *EGFR* signaling by regulating membrane phospholipid dynamics and is implicated as a glioma therapeutic vulnerability[75]. *L_salmon4* also included four peaks linked to *NOVA1,* an evolutionarily conserved splicing regulator in the developing nervous system. *ELOVL2* and *NOVA1* were located in open ‘A’ chromatin compartments specifically in *EGFR*-amplified samples (Fig 6J). We thus reveal alterations in GBM chromatin landscape associated with *EGFR* amplification, providing support for therapeutic targeting the *ELOVL2* metabolic network and unveiling additional genes epigenetically upregulated in *EGFR*-amplified regions for further investigation.

Finally, we characterized chromatin programs with differential spatial enrichment across tumors. *L_mediumorchid* was enriched towards the periphery (R_d +0.39) and contained regulatory elements of genes involved in neuron projections including 9 linked to *ARPP21*,

which controls dendritic branching[76] (Fig S6I–J). Modules enriched towards the tumor core – *A_lavenderblush3* (R_d −0.48), *L_lightcyan1* (−0.45), *L_orangered3* (−0.36), *L_thistle* (−0.36) – all showed AP-1 or its component FOSL2 as the top enriched motif (Fig 5G). *A_lavenderblush3* had 28 constituent peaks that included two enhancers of *GADD45B,* which is upregulated in stressful conditions, and enhancers of *LGALS3* and *ANGPTL4*, both of which promote treatment resistance in GBM[77,78]. *L_orangered3* included regulatory elements of AP-1 components *FOSL2* and *JUN* as well as of stress and hypoxia response genes *HSPA5, ERFFI1,* and *HIF1A* (Fig S6K). These modules showed heterogeneity amongst cells from individual samples (Fig 6K) and were enriched in cells in the MES-like state (Fig S6H). Whole-tumor analysis of GBM transcriptomes and chromatin landscapes thus independently identifies neuronal hijacking at the tumor periphery and AP-1-mediated mesenchymal differentiation within the tumor core. These complementary analyses reveal specific genes and regulatory machinery associated with each of these programs for further mechanistic and therapeutic investigation.

Discussion

A whole-tumor perspective of GBM

GBM treatment options remain limited and prognosis dismal despite decades of molecular investigation. The first landmark TCGA publication focused on GBM[7] as have follow-up studies with expanded patient cohorts and additional data types and analyses[4–6]. While this cohort view of GBM has established genes and pathways commonly altered across patients, it is not designed for deciphering molecular roots of individual tumors and understanding evolutionary dynamics by which they become heterogeneous and treatment-resistant. The 3D spatial sampling approach we have presented allows GBM to be studied from a whole-tumor perspective. By quantifying and accounting for sample purity in our analyses, we distinguish tumor cell-intrinsic genomic and epigenomic alterations and differences in program activation from differences in cell type composition. We can then differentiate molecular events that are tumor-wide versus heterogeneous and thus infer GBM evolutionary trajectories. Tumor-wide activation of specific neurodevelopmental programs sheds new light on the longstanding question of GBM cell-of-origin[79–84]. *EGFR* is expressed in cells along the lineage trajectory of oRG differentiation to OPCs[63], indicating a plausible mechanism of tumor initiation whereby gain of chr7 containing *EGFR, PTPRZ1,* and *PTN* locks cells into an undifferentiated IPC/pre-OPC transit-amplifying state. Gains of chr7 are less frequent in GBM with primitive neuronal component[27] in which we find activation of programs from the distinct lineage trajectory of IPC differentiation to neurons. The fortuitous inclusion of this GBM variant in our cohort provides a striking contrast that divulges its divergent origins as well as its regulatory network and master regulators. Cell-of-origin of other GBM histological variants or tumor types may be similarly discerned by whole-tumor sampling and identification of programs active tumor-wide.

By delineating genes and regulatory elements comprising programs from GBM origins, we discover tumor-wide therapeutic targets that may avoid heterogeneity-related failures. These include novel targets and those such as *KIF18A* and *PTPRZ1* that have been evaluated to some extent[60,61,65–67], but without knowledge of their tumor-wide activation. While most

GBMs share a common cellular origin, their genetic roots are deeply personalized. Our findings provide impetus for searching for chromothripsis and other early SVs in patients upon diagnosis as these massively disrupt the genome and epigenome and give rise to tumor-wide fusions that provide opportunities for precision molecular and immunotherapeutic targeting.

Redefining GBM heterogeneity in 3D space

Molecular studies of GBM have classified patients, samples, and now individual cells to subtypes or states[5,6,10,12–14]. Heterogeneity has been defined by inconsistencies in classification and tumor evolution by transitions observed between subtypes or states[8,12,16,17]. By directly interrogating GBM evolution and heterogeneity in whole tumors, we find that these concepts are better understood through modular activation of specific tumor and microenvironmental programs occurring independently or together in different patients, tumor regions, and individual cells. By analyzing co-variation across GBM transcriptomes and chromatin landscapes, we have delineated genes and regulatory elements comprising distinct tumor and microenvironmental programs and have defined their inter- and intratumoral heterogeneity from 3D whole-tumor to single-cell resolution (Fig 7A–B). While many programs are independently detected by our chromatin and transcriptomic analyses, others are uniquely detected by one, thus underscoring the value of combining both to capture the full extent of heterogeneity. Low-abundance cell types such as T cells are detected only by transcriptomic analysis likely because individual cells can produce large numbers of transcripts, but only have a diploid genome on which chromatin accessibility can be assessed. In contrast, tumor programs driven by NEUROD1 and NFIA are detected only by chromatin analysis likely because they bind and alter accessibility of large numbers of sites throughout the genome while effects on transcription are relatively subtle. During development, NEUROD1 and NFIA drive differentiation towards neuronal and astrocytic fates respectively and their activation is under precise spatiotemporal control. In GBM, these programs can become aberrantly and concurrently active as in P500 in which we find tumor-wide activation of oRG to OPC, NEUROD1-mediated neuronal, and NFIA-mediated astrocytic differentiation programs (Fig 7C). Aberrant activation of neurodevelopmental programs can also drive intratumoral heterogeneity as in P521 in which NFIA-mediated astrocytic differentiation occurs only in the *EGFR*-amplified tumor region. *EGFR* amplification is itself associated with an epigenomic program active tumor-wide as in P500 or with intratumoral heterogeneity as in P521.

3D spatial analysis reveals distinct microenvironments in the GBM core and periphery, formation of which is attributed to differential distribution of nonmalignant cell types and to tumor cell-intrinsic programs that become activated in response to these nonmalignant cell types or other regional factors such as injury and hypoxia. Neuronal hijacking occurs at the GBM periphery where tumor cells functionally interact with neurons. Inside the tumor core, we discover either immune-hot microenvironments with interferon signaling and T cell infiltration or immune-cold microenvironments undergoing mesenchymal differentiation programs coordinately activated across tumor, immune, and stromal cell types by master regulator AP-1.

A 3D spatially annotated resource

The unique 3D spatially-resolved maps of whole GBM tumors we have generated can be publicly accessed on our online interactive platform. Users can select any gene, transcriptomic or chromatin program, or other feature-of-interest to visualize its spatial pattering in 360° across individual tumors and generate summary figures and statistics showing its spatial proclivities with regards to the tumor centroid, periphery, and contrast-enhancing lesion. The insights we have drawn from redefining GBM evolution and heterogeneity from a 3D whole-tumor perspective, and the insights that will follow from studies taking advantage of our newly established resource, have the potential to impact clinical care and outcomes.

Limitations of the study

In vitro and *in vivo* experiments are a necessary next step to test inferences on GBM origins, plasticity, and vulnerabilities. With regards to origins, malignant transformation in the specific lineage trajectories we have identified could be tested in cell and organoid models of human neurodevelopment[63,65,85,86], potentially giving rise to new tumor models that more accurately recapitulate GBM. Model systems could also be used to test roles of NEUROD1, NFIA, and other factors in altering GBM chromatin landscapes and driving cell state transitions. Our analyses have revealed a wealth of tumor-wide candidate therapeutic targets that can avoid heterogeneity-related failures as well as novel candidate biomarkers and therapeutic targets associated with neuronal hijacking, formation of immune-hot and cold microenvironments, and other programs we have defined. For example, the top-ranked gene in *R_midnightblue LRRC25* is a negative regulator of innate immune signaling[52,53] and may potentially be targeted to reverse the immunosuppressive state of microglia. We have curated a list of such genes for follow-up investigation in appropriate experimental and preclinical models (Table S8).

STAR Methods

RESOURCE AVAILABILITY

Lead contact—Further information and requests for resources should be directed to and will be fulfilled by the lead contact, Dr. Joseph Costello (Joseph.Costello@ucsf.edu).

Materials availability—This study did not generate unique new reagents.

Data and code availability

- All exome, RNA-Seq, ATAC-Seq, and Hi-C datasets have been deposited in the European Genome-Phenome Archive (EGA) database under accession number EGAS00001006785, EGAD00001005221/2, and EGAD00001009496/7. Processed single-cell ATAC-Seq datasets have been deposited in GEO under the accession number GSE226726. This paper additionally analyzes existing, publicly available data. These accession numbers for the datasets are listed in the key resources table.

- All original R code has been deposited at https://github.com/radhikamathur/3DSpatiallyMappedGBMs and is publicly available as of the date of publication.
- Any additional information required to reanalyze the data reported in this paper is available from the lead contact upon request.

EXPERIMENTAL MODEL AND STUDY PARTICIPANT DETAILS

Sample use was approved by the University of California San Francisco's Committee on Human Research and the University of California, San Francisco's Institutional Review Board. All patients provided informed written consent. The age, sex, race, and ethnicity of all 11 study participants is provided in Supplementary Table 1.

METHOD DETAILS

Acquisition of 3D spatially mapped GBM samples—Neurosurgeons and study co-authors (S.H.J., M.S.B) conducted standard-of-care surgical resections [87,88] and progressively harvested glioblastoma specimen at their discretion with the goal to represent spatially distant intratumoral regions. Intraoperative brain mapping was used to identify regions of functional significance, allowing safe acquisition of samples from gliomas in many cortical and subcortical locations including both dominant and non-dominant hemispheres. Stereotactic site-directed biopsies from intratumoral regions were taken and the location of each sample was recorded as a set of LPS coordinates registered to a preoperative MR image using a Brainlab pointer and Brainlab Cranial Navigation software (v3; BrainLAB AG). A UCSF Brain Tumor Center Biorepository staff member was present in the operating room to acquire blood from existing lines prior to skull opening and for tissue acquisition following strict standard operating procedures to optimally preserve the biospecimen. Once acquired, biopsies were placed on wet-ice and transported to the laboratory, where they were divided so that 2/3 was flash-frozen in liquid nitrogen and 1/3 was fixed in 10% neutral-buffered formalin for 8–14 hours, processed, and paraffin-embedded (FFPE material). Flash-frozen tissue was further divided when tissue size permitted for DNA/RNA extraction, ATAC-Seq (tissue and/or single-cell), and Hi-C. Sample information including analyses performed are provided in Supplementary Table S1.

3D modeling and spatial analysis—Image registration was performed to the pre-operation T_1-weighted post-gadolinium series using FLIRT (FMRIB's Linear Image Registration Tool) package [89,90]. Brain extraction from the T_2-weighted FLAIR image stack was performed using FSL's BET[91]. Volumetric tumor ROIs were drawn for each tumor from the T_2-weighted hyperintense region and from the contrast enhancing lesion. 5mm spherical ROIs were generated for each sample coordinate and converted to DICOM format for visualization and downstream analysis. DICOM files corresponding to the extracted brain, tumor ROIs, and sample ROIs were imported into freely available software Slicer[92]. Volumetric 3D models of the brain, tumor, and sample ROIs were generated using Slicer's Grayscale Model Maker module. The composite 3D model is viewable within Slicer or an exported 3D video made using the ffmpeg (https://www.ffmpeg.org/) executable. Rotating 3D models for each patient showing sample location in context of the whole tumor and contrast-enhancing lesions are provided in Supplementary Video S1 in .mp4 format. For 3D

spatial analysis, DICOM files corresponding to tumor and sample ROIs were imported into R using the oro.dicom package. Distances between sample pairs and minimum distances from each sample to the tumor centroid (d_c) and periphery (d_p) were calculated using the Cartesian coordinate system. Frontal and temporal regions from P530 were treated independently for calculations of inter-sample distances and relative distances from centroid and periphery. The inter-sample distance matrix and related calculations are provided in Supplementary Table S2.

Histopathological analysis—Tumor tissue targets were fixed in 10% neutral-buffered formalin, processed, and embedded in paraffin. Tumor sections (5 μm) were prepared and stored at −20°C prior to use. Slides were stained with hematoxylin & eosin (H&E) or immunostained. Notes from histopathological analysis on each sample including presence of necrosis and blood vessel hyperplasia are provided in Supplementary Table S1. All single and multiplex immunostainings were performed using a Discovery XT autostainer (Ventana Medical Systems, Inc., USA). For signal detection, the Multimer HRP kit (Ventana Medical Systems, Inc., USA) followed by either DAB or fluorescent detection kits were used. Fluorophores with the least autofluorescence on FFPE tissue were selected to minimize false positives: Cyanine 5 (Cy5) (DISCOVERY CY5 Kit, Cat#760238, Roche Diagnostics Corporation, Indianapolis, USA), rhodamine (DISCOVERY Rhodamine Kit, Cat#760233, Roche Diagnostics Corporation, Indianapolis, USA), and FITC (DISCOVERY Rhodamine Kit, Cat#760233, Roche Diagnostics Corporation, Indianapolis, USA). Slides were then counterstained with DAPI (Sigma Aldrich, USA) at 5 μg/ml in PBS (Sigma Aldrich, USA) for 15 minutes, mounted with prolong Gold antifade mounting media reagent (Invitrogen, USA) and stored at −20°C prior to imaging. Positive and negative controls were included for each marker. Images of stained slides were acquired using either a light microscope (Olympus BX41 microscope using UC90 Cooled CCD 9 Megapixel camera) or Zeiss Cell Observer epifluorescence microscope equipped with an AxioCam 506M camera and an Excellitas X-Cite 120Q light source. Primary antibodies used and conditions were CD163 (Catalog # CD163-L-CE, Leica Biosystems, USA; mouse clone 10D6; dilution 1:500); IBA1 (Catalog#019-19741, Wako Chemicals USA, polyclonal rabbit, dilution 1:500); CD204 (Catalog # KMU-MA01, Cosmo Bio USA, clone SRA-E5, dilution 1:100); CD3 (Catalog #NCL-L-CD3-565, Leica Biosystems, clone LN10, dilution 1:100); and PTPRZ1 (Catalog #610179, BD Biosciences, dilution 1:600).

UCSF500 Clinical NGS panel—Targeted next-generation sequencing (NGS)[93] was conducted on a single diagnostic tissue biopsy sample from each tumor. UCSF500 Version 2 with NimbleGen baits targeting of 479 cancer genes with select intronic and upstream regulatory regions of 47 genes was utilized for all patients except P529 and P530. UCSF500 Version 3 with IDT baits targeting 529 genes with 73 select intronic and upstream regulatory regions was utilized for these two patients. Sequencing of captured libraries was performed on Illumina HiSeq 2500 or NovaSeq 6000. Sequence reads were de-duplicated to allow for accurate allele frequency determination and copy number calling and were aligned to the human reference sequence UCSC build hg19 (NCBI build 37) for variant calling. This test was developed and its performance characteristics determined by the UCSF Clinical Cancer Genomics Laboratory, which is certified by the Clinical Laboratory Improvement

Act of 1988 (CLIA certified). Summaries of each patient's UCSF500 report are provided in Supplementary Table S3.

Exome-sequencing—Genomic DNA and RNA were simultaneously extracted from fresh-frozen tissue using the AllPrep DNA/RNA/miRNA Universal Kit (QIAGEN). Exome capture was performed using the Agilent SureSelect Target Enrichment System Protocol (Version 1.0, September 2009) and Nimblegen SeqCap EZ Exome v3. Sequencing was conducted using HiSeq4000 or NovaSeq (Illumina). Exome data was processed as previously described by our group[94] with further filtering applied to mark "discard" variants from repeat or low-quality regions of the genome. For phylogenetic trees, a binary call matrix to calculate Manhattan distance and fasteme.ols from R package ape[95] was used to construct rooted binary trees. Allele-specific copy-number alterations were profiled using the FACETS algorithm[96]. PyClone VI (v0.1.0)[20] (https://github.com/Roth-Lab/pyclone-vi) was used to infer clonal structure from allele frequencies as determined by MuTect and copy number alterations estimated by FACETS. PyCloneVI was run a minimum of 3 times to assess the stability of the number of clusters estimated. Results from PyCloneVI and FACETS copy number analysis from each patient are provided in Supplementary Table S3.

Purity estimation—Each lane of exome sequencing reads was aligned against human genome reference build GRCh38 released by the Broad Institute on July 12, 2016 using BWA-MEM2 (v2.2.1). BAM files were sorted by query name using SAMtools (v1.15.1)[97] and then duplicated reads were marked with Genome Analysis Toolkit (GATK) MarkDuplicatesSpark (GATK v4.2.4.1)[98]. In addition, Indel realignment GATK (v3.7.0) was performed to process multiple tumor samples and paired normal sample together per patient. Then, Base Quality Score Recalibration (BQSR) was run on the realigned sample BAMs using GATK (v4.2.4.1). Separate normal and tumor sample BAMs were generated and their headers were corrected using SAMtools (v1.12). Tumor purity was inferred using HATCHet (v0.4.14)[99]. The GATK processed normal/tumor sample BAMs were jointly processed per patient. dbSNP build 151 was used as a reference SNP list. As recommended for WES by the developer, the bin size calculating for Read Depth Ratio (RDR) and B-allele frequency (BAF) was set at 250kb. Read-count thresholds were set at a minimum coverage of 20 and a maximum coverage of 5,000 based on the average coverage of the samples and also to allow detection of high copy number alterations. Bootstrapping for clustering was performed with the recommended values of `bootclustering = 20`, `ratiodeviation = 0.002` and `bafdeviation = 0.002`. Also, the maximum copy number for diploid and tetraploid was set at 25 and 50, respectively to allow detection of high copy numbers (`diploidcmax = 25`, `tetraploidcmax = 50`). Lastly, Gurobi solver was used to detect 2 to 8 clones (`clones = 2,8`). Purity estimates are provided in Supplementary Table S1.

RNA-sequencing—Strand-specific transcriptome sequencing libraries were prepared using the KAPA Stranded mRNA-Seq Kit (KR0960-v2.14, Kapa Biosystems). Trim Galore (https://www.bioinformatics.babraham.ac.uk/projects/trim_galore/) was first used to apply quality and adapter trimming to raw fastq files. Trimmed reads were then mapped to hg19 human reference genome build using STAR program[100]. Genes and transcripts quantification were done by RSEM program[101]. Tpm (transcripts per million) value for

each gene was transformed to log2(tpm+1) and then quantile normalized across all samples. The normalized log2(tpm+1) values were used for further analysis and are provided in Supplementary Table S5.

Chromatin accessibility profiling (ATAC-Seq)—ATAC-Seq on frozen primary GBM tissues was conducted as described by Corces et al[102] with samples from the same patient processed in parallel. Nuclei were isolated from frozen tissues by Dounce homogenization followed by density gradient centrifugation. Transposition reactions were conducted with Illumina Tagment DNA TDE1 Enzyme and Buffer Kits using ~50,000 nuclei per reaction. Reactions were carried out in duplicate for all samples except those from P530. Transposed fragments were amplified by qPCR with NEBNext Master Mix and SYBR Green. Libraries were quantified with the KAPA Library Quantification kit and nucleosomal banding patterns were confirmed with Agilent Bioanalyzer DNA 1000. Paired-end sequencing (PE150) was conducted using the Illumina Hi-Seq or Nova-Seq (for samples from P530).

Raw fastq files were trimmed by Trim Galore. Then we used the standard ENCODE ATAC-Seq pipeline (https://github.com/ENCODE-DCC/atac-seq-pipeline) for reads mapping and peak calling. Reads were mapped against the hg19 human reference genome build using Bowtie2 aligner[103]. The resulting raw bam files were further filtered by mappability and quality. ATAC-Seq peaks were called from filtered bam files using MACS2 with default parameters[104]. For samples that have replicates (all patient samples except P530), we used the overlap optimal narrow peaks between replicates. We filtered the peaks using MACS2 output −log10pvalue > 5 and −log10qvalue > 2 criteria to get confident peaks. Each ATAC-Seq peak was trimmed to 500bp, with 250bp extended on either side of the peak summit. ATAC-Seq peaks of the 70 samples were merged into a merged peak set. During the peak merging, if multiple peaks have overlap, the peak with highest normalized peak score were picked. Here normalized peak score refers to the −log10pvalue of a peak normalized by the sum of all of the peak scores in a given sample. Reads counts within each peak of the merged peak set were calculated from bam files using deepTools[105]. Cpm value was then calculated using the edgeR package[106] and transformed to log2(cpm+1) and quantile normalized across all samples. The normalized log2(cpm+1) values were used for further analysis.

Promoters were defined as ATAC-Seq peaks from the merged set with summits within −1KB and 100bp of the gene transcription start sites (TSS). Enhancers were defined as ATAC-Seq peaks that did not overlap with the promoter region and peak-to-gene linkage prediction was performed as described by Corces et al[102]. Correlation between log2(cpm+1) value of distal ATAC-Seq peaks and log2(tpm+1) value of gene expression was calculated for all distal ATAC-Seq peaks and genes within 0.5Mb. FDR less than 0.05 was used as cutoff to identify significant linkages. Peak-gene linkages and normalized log2(cpm+1) values are provided in Supplementary Table S6.

Single-nucleus ATAC-Seq sample preparation and analysis—Samples were obtained either as previously cryopreserved extracted nuclei (P519, P521) or as individually snap-frozen tissue fragments (P524, P529). Frozen tissue samples were processed using an iodixanol gradient centrifugation method adapted from Corces et al[102], with dounce

homogenization and centrifugation. Extracted nuclei were washed 1x in 10X wash buffer and resuspended in 100 uL of 0.1X 10X lysis buffer for 2 minutes, followed by a second wash and resuspension into 10X nuclear buffer. Downstream sample processing and library construction was performed using the Chromium NextGEM Single Cell ATAC Kit v2 (10X Genomics), targeting the maximum number of nuclei per sample, up to a max limit of 8000 nuclei.

Libraries were sequenced at the University of Calgary Centre for Health Genomics and Informatics (CHGI) on an Illumina NovaSeq 6000 sequencer in paired-end mode, targeting 50,000 reads per cell. Sequencing data was processed using the 10X pipeline and CellRanger ATAC-1.2.0. Downstream matrices were processed using Signac 1.6.0[107]. Samples were thresholded using the following parameters: retention of cells and features present in at least 10 cells, peak_region_fragments > 3000, pct_reads_in_peaks > 15, blacklist_ratio < 0.05, lowmapq < 30000. Samples from the same patient were merged together, and normalized by dividing all counts by the mean signal across 5000 randomly selected peaks to account for differences in transposition efficiency and sequencing depth between samples. Dimension reduction was performed using latent semantic indexing (LSI) followed by UMAP construction using LSI components 2:30 and the following parameters: n.neighbours=71L, min.dist=0.4, spread=1.5, repulsion.strength=1.1, and calculation of clusters using Louvain clustering with default parameters. Copy number inference and putative ecDNA detection was performed using Copy-scAT with default parameters[108] followed by calculation of consensus CNVs by taking the rounded value of the 60th quantile value of each CNV for each cluster. Motif analysis was performed using ChromVAR[109]. Gene activity scores were calculated using the Signac GeneActivity function using the Ensembl v86 database. Per-cell scores for modules, linkage modules and gene scores were calculated as follows. For peak-based metrics (modules, linkage modules) bulk ATAC peak lists were converted from hg19 to hg38, and matching peaks in the snATAC-seq datasets were identified using the GenomicRanges findOverlaps function. Peaks with a total normalized intensity of at least 100 across each merged patient sample were retained and a mean score across each signature was computed for each cell. A similar approach was used for RNA gene scores, which were cross-referenced to genes in the normalized GeneActivity matrix. Gene names from the GeneActivity object were converted using the HGNChelper package to match updated HGNC symbols in the peak lists. Information on individual cells including neoplastic status, gene activity scores, and read-in-peak scores are provided in Supplementary Table S7.

Hi-C sample preparation and data analysis—Hi-C was conducted using spatially mapped samples from P524, P529, and P530 and bulk tumor tissue for remaining patients. Tissue samples were frozen with liquid nitrogen, pulverized using mortar and pestle until the sample resembles a fine powder, and then cross-linked using 2% formaldehyde. Hi-C libraries were generated and quality-checked per manufacturer's protocol (ARIMA Genomics). As per their protocol, we tested and did QC on samples and sequenced 500M–1200M reads for each sample using Illumina's NovaSeq platform (Illumina).

Raw fastq files were first trimmed by Trim Galore and then mapped to hg19 human reference genome using runHiC pipeline (based on 4DN consortium)[110]. Pair-end

sequencing data were mapped by bwa aligner[111]. Aligned read pairs that have PCR duplicates or map to the same restriction fragment were filtered out. Reads were binned at 5 kb resolution and the contact matrix was stored in a cool file. The run-cool2multirescool script from 4DN consortium was then used to generate the multi-resolution cool files (5kb, 10kb, 25kb, 40kb, 50kb, 100kb, 250kb, 500 kb, 1Mb, 2.5Mb, 5Mb, and 10 Mb) and perform ICE normalization. Multi-resolution .hic files were also generated using Juicer tools[112] and can be visualized in Juicebox directly.

Loop calling in each Hi-C sample was performed using Peakachu[113], which utilizes Random Forest classification framework. For each sample, we calculated the total number of intra-chromosomal pairs and then selected the most appropriate pre-trained model for loop prediction. A/B compartment was calculated at 100kb resolution using cooltools[114]. Structure variations were predicted by EagleC[29], which combines deep-learning and ensemble-learning strategies. We first used NeoLoopFinder[115] toolkit to calculate the copy number variation profile and remove the copy number variation effects. Then we called SVs using EagleC with “--balance-type CNV” parameters under 5kb, 10kb, and 50kb resolutions. Results from the three resolutions were combined in a non-redundant manner. The reconstructed Hi-C map was then generated by NeoLoopFinder. Structural variant lists are provided in Supplementary Table S4.

Fusion gene identification and validation—Fusion genes were identified in RNA-Seq data using Arriba software[116]. Validation of fusion genes was conducted by reverse transcription polymerase chain reaction (RT-PCR), gel extraction, and Sanger sequencing. RNA was isolated with the Qiagen AllPrep DNA/RNA/miRNA Universal Kit (Cat.80224) according to manufacturer’s protocol. Briefly, 1000 ng of DNase-treated RNA was converted to cDNA using the iScript cDNA Synthesis Kit (BioRad, #1708891). This cDNA was then diluted 1:5 using nuclease free water, and 2 µl of this diluted cDNA was used for PCR reactions using the Phusion Green High-Fidelity DNA Polymerase (Thermo Scientific, #F-534L) with HF buffer. Cycling conditions were an initial step of 98 °C for 30 seconds, followed by 35 cycles of 98 °C for 10 seconds, the primer pair specific annealing temperature for 20 seconds, and 72 °C for 30 seconds, with a final elongation step of 72 °C for 5 minutes. Gene fusion specific primer sets were designed using NCBI Primer Blast (J.Ye et al. 2012) and an M13 forward sequence (5’-GTAAAACGACGGCCAG-3’) was added to the 5’ end of the forward primer and an M13 reverse sequence (5’-CAGGAAACAGCTATGAC-3’) was added to the 5’ end of the reverse primer. A negative control PCR reaction without template was included for each primer pair. PCR products were separated on a 1% agarose gel, excised, and gel purified (NEB, #T1020). Sample concentrations were then determined via Nanodrop (Thermo Scientific) and were submitted for Sanger sequencing (GENEWIZ) with M13F and M13R sequencing primers. Primers used for RT-PCR and results from Sanger sequencing are provided in Supplementary Table S4.

Characterization of gene fusion-derived neoantigens and HLA presentation prediction—Amino acid sequences identified by Arriba-detected gene fusion events were partitioned into multi-mer sequences of 8, 9, 10, and 11 amino acids in length.

Cross validation was next performed with normal tissue-expressing amino acid sequences utilizing a reference human proteome dataset (UniProt, Proteome ID: UP000005640) to select for cancer-specific peptide sequences. OptiType was next utilized on patient-derived whole-exome sequencing data to identify all major and minor HLA Class I alleles[117]. To predict personalized immunogenic targets generated independently within the patient cohort, HLA-restricted presentation scores for all cancer-nmers were assigned based on the binding affinity of each patient's corresponding HLA Class I repertoire. Peptide:HLA presentation was predicted using a combination of HLAthena [39]and MHCFlurry 2.0[118]. Cancer-specific multi-mers along with the upstream and downstream flanking sequences were used as input sequences for both algorithms. HLAthena MSiC analysis was performed with a threshold of 0.1, aggregation by peptide, and assignment of peptides to alleles by rank. MHCFlurry 2.0 analysis was initiated with the models_class1_presentation baseline parameters. Cancer-specific multimers were independently ranked based on presentation scores, and multi-mers found in the upper 10th percentile of candidates in both algorithms are predicted neoantigens with increased likelihood for HLA presentation. These cancer-specific multimers in conjunction with flanking upstream and downstream sequences were mapped back to their corresponding gene fusion events.

Transcriptome unsupervised covariation analysis—Weighted correlation network analysis was performed as described in our previous work on human brain tissues[41]. Genome-wide biweight midcorrelations (bicor) were calculated using the WGCNA R package[119] on RNA-Seq data from 69 spatially mapped GBM samples from 8 patients. All genes were clustered using the flashClust[119] implementation of hierarchical clustering with complete linkage and 1 – bicor as a distance measure. Each resulting dendrogram was cut at a static height (0.624) corresponding to the top 5% of values of the correlation matrix for case one and case two, respectively. All clusters consisting of at least 20 members were identified and summarized by their module eigengene[120,121] (i.e. the first principal component obtained by singular value decomposition) using the moduleEigengenes function of the WGCNA R package. Highly similar modules were merged based if the Pearson correlation of their module eigengenes was >0.85. This procedure was performed iteratively such that the pair of modules with the highest correlation > 0.85 was merged, followed by recalculation of all module eigengenes, followed by recalculation of all correlations, until no pairs of modules exceeded the threshold. The WGCNA measure of module membership, kME, was calculated for all genes with respect to each module. kME is defined as the Pearson correlation between the expression pattern of a gene and a module eigengene and therefore quantifies the extent to which a gene conforms to the characteristic expression pattern of a module[121]. For downstream analyses, module definitions were expanded to include all genes with significant kME values, with significance adjusted for multiple comparisons by Bonferroni correction. If a gene was significantly correlated with more than one module, it was assigned to the module for which it had the highest kME value. Gene set enrichment analysis was performed for all modules using a one-sided Fisher's exact test as implemented by the fisher.test R function. Network analysis and visualization was conducted using StringApp[122] on Cytoscape (version3.9.1). Summary information on each module, lists of constituent genes ranked by significance, and signatures used for enrichment analysis are provided in Supplementary Table S5.

Chromatin landscape unsupervised covariation analysis—Weighted correlation network analysis was conducted as above on ATAC-Seq data from the same 69 spatially mapped samples from 8 GBM patients. Modules were derived independently from the top 20% most variable peaks from the merged list (ATAC modules) and from the subset of peaks from the merged list that were defined as promoters or enhancers linked to one or more genes (Linkage Modules). Static heights of 0.65 and 0.34 and minimum sizes of 20 and 30 were used to derive ATAC and Linkage Modules, respectively. The WGCNA measure of module membership, kME, was calculated for all peaks with respect to each module. For downstream analyses, module definitions were expanded to include all peaks with significant kME values, with significance adjusted for multiple comparisons by Bonferroni correction. TF enrichment analysis was performed on constituent peaks from each module using HOMER[123]. TF footprinting analysis was performed using HINT-ATAC[124]. Bam files and peak files of each sample were provided as input. Summary information on each module, lists of constituent peaks ranked by significance, and top-linked genes are provided in Supplementary Table S6.

QUANTIFICATION AND STATISTICAL ANALYSIS

Quantification and statistical analyses were conducted using the ggplot2, ggpubr (version 0.4.0), and EnvStats R packages. Statistical significance of differences in means was evaluated by T-tests in Fig 1B, 1H, 2H, 2K, 4I, 6F, 6I and by ANOVA in Fig 4B. Linear regression models were fitted and evaluated by Pearson correlation in Fig 1C, 4E, 5A, 5C, 5H, 6H, S1A, S2C, S4C, S5A, S6A, S6I. R code used to generate figures and conduct statistical analysis is available on Github (https://github.com/radhikamathur/3DSpatiallyMappedGBMs).

ADDITIONAL RESOURCES

Interactive 3D visualization and exploration of datasets, including single-nucleus ATAC data, is available at http://3D-gbms.shinyapps.io/search/.

Supplementary Material

Refer to Web version on PubMed Central for supplementary material.

Acknowledgments

We thank the patients and their families for consent to collect and use tumor samples. We thank the staff of the University of California, San Francisco's Brain Tumor Center Tissue Bank for sample acquisition and histopathology services and the Center for Advanced Technology for sequencing services. This project was supported by a gift from the Hana Jabsheh Research Initiative and the Panattoni family. Additional support provided by the Brain Tumor Funders Collaborative (J.F.C.), National Institutes of Health Grants F32 1F32CA239472-01 (R.M), T32 T32CA151022 (R.M., S.H.), R01 CA169316 (to J.F.C.), P01 CA118816-06 (to J.F.C., J.M.L, J.J.P.), R50 CA274229 (to C. H.), P50 CA097257 (to J.J.P., and J.F.C.), U01 CA229345 (to J.J.P.); and the Chan Zuckerberg (CZ) Biohub. F.Y. was supported by NIH grants R35GM124820, 1R01HG009906, and R01HG011207.

References

1. Black JRM, and McGranahan N (2021). Genetic and non-genetic clonal diversity in cancer evolution. Nat. Rev. Cancer, 1–14. 10.1038/s41568-021-00336-2. [PubMed: 33203999]

2. Nicholson JG, and Fine HA (2021). Diffuse Glioma Heterogeneity and Its Therapeutic Implications. Cancer Discov. 11, 575–590. 10.1158/2159-8290.CD-20-1474. [PubMed: 33558264]

3. Marusyk A, Janiszewska M, and Polyak K (2020). Intratumor Heterogeneity: The Rosetta Stone of Therapy Resistance. Cancer Cell 37, 471–484. 10.1016/j.ccell.2020.03.007. [PubMed: 32289271]

4. Brennan CW, Verhaak RGW, McKenna A, Campos B, Noushmehr H, Salama SR, Zheng S, Chakravarty D, Sanborn JZ, Berman SH, et al. (2013). The Somatic Genomic Landscape of Glioblastoma. Cell 155, 462–477. 10.1016/j.cell.2013.09.034. [PubMed: 24120142]

5. Ceccarelli M, Barthel FP, Malta TM, Sabedot TS, Salama SR, Murray BA, Morozova O, Newton Y, Radenbaugh A, Pagnotta SM, et al. (2016). Molecular Profiling Reveals Biologically Discrete Subsets and Pathways of Progression in Diffuse Glioma. Cell 164, 550–563. 10.1016/j.cell.2015.12.028. [PubMed: 26824661]

6. Verhaak RGW, Hoadley KA, Purdom E, Wang V, Qi Y, and Wilkerson MD (2010). Integrated genomic analysis identifies clinically relevant subtypes of glioblastoma characterized by abnormalities in PDGFRA, IDH1, EGFR, and NF1. Cancer Cell 17, 98–110. 10.1016/j.ccr.2009.12.020. [PubMed: 20129251]

7. The Cancer Genome Atlas Research Network (2008). Comprehensive genomic characterization defines human glioblastoma genes and core pathways. Nature 455, 1061–1068. 10.1038/nature07385. [PubMed: 18772890]

8. Sottoriva A, Spiteri I, Piccirillo SG, Touloumis A, Collins VP, Marioni JC, Curtis C, Watts C, and Tavaré S (2013). Intratumor heterogeneity in human glioblastoma reflects cancer evolutionary dynamics. Proc. Natl. Acad. Sci. U. S. A. 110, 4009–4014. 10.1073/pnas.1219747110. [PubMed: 23412337]

9. Puchalski RB, Shah N, Miller J, Dalley R, Nomura SR, Yoon J-G, Smith KA, Lankerovich M, Bertagnolli D, Bickley K, et al. (2018). An anatomic transcriptional atlas of human glioblastoma. Science 360, 660–663. 10.1126/science.aaf2666. [PubMed: 29748285]

10. Wang Q, Hu B, Hu X, Kim H, Squatrito M, and Scarpace L (2018). Tumor Evolution of Glioma-Intrinsic Gene Expression Subtypes Associates with Immunological Changes in the Microenvironment. Cancer Cell 33, 152. 10.1016/j.ccell.2017.12.012. [PubMed: 29316430]

11. Patel AP, Tirosh I, Trombetta JJ, Shalek AK, Gillespie SM, and Wakimoto H (2014). Single-cell RNA-seq highlights intratumoral heterogeneity in primary glioblastoma. Science 344, 1396–1401. 10.1126/science.1254257. [PubMed: 24925914]

12. Neftel C, Laffy J, Filbin MG, Hara T, Shore ME, and Rahme GJ (2019). An Integrative Model of Cellular States. Plast. Genet. Glioblastoma Cell, 1–37. 10.1016/j.cell.2019.06.024.

13. Garofano L, Migliozzi S, Oh YT, D'Angelo F, Najac RD, and Ko A (2021). Pathway-based classification of glioblastoma uncovers a mitochondrial subtype with therapeutic vulnerabilities. Nat. Cancer, 1–38. 10.1038/s43018-020-00159-4. [PubMed: 35121896]

14. Richards LM, Whitley OKN, MacLeod G, Cavalli FMG, Coutinho FJ, and Jaramillo JE (2021). Gradient of Developmental and Injury Response transcriptional states defines functional vulnerabilities underpinning glioblastoma heterogeneity. Nat. Cancer, 1–40. 10.1038/s43018-020-00154-9. [PubMed: 35121896]

15. Ravi VM, Will P, Kueckelhaus J, Sun N, Joseph K, Salié H, Vollmer L, Kuliesiute U, von Ehr J, Benotmane JK, et al. (2022). Spatially resolved multi-omics deciphers bidirectional tumor-host interdependence in glioblastoma. Cancer Cell 40, 639–655.e13. 10.1016/j.ccell.2022.05.009. [PubMed: 35700707]

16. Chaligne R, Gaiti F, and Silverbush D (2021). Epigenetic encoding, heritability and plasticity of glioma transcriptional cell states. Nat Genet 53, 1469–1479. 10.1038/s41588-021-00927-7. [PubMed: 34594037]

17. Johnson KC, Anderson KJ, and Courtois ET (2021). Single-cell multimodal glioma analyses identify epigenetic regulators of cellular plasticity and environmental stress response. Nat Genet 53, 1456–1468. 10.1038/s41588-021-00926-8. [PubMed: 34594038]

18. Molinaro AM, Hervey-Jumper S, Morshed RA, Young J, Han SJ, and Chunduru P (2020). Association of Maximal Extent of Resection of Contrast-Enhanced and Non-Contrast-Enhanced Tumor With Survival Within Molecular Subgroups of Patients With Newly Diagnosed Glioblastoma. JAMA Oncol. 6, 495–503. 10.1001/jamaoncol.2019.6143. [PubMed: 32027343]

19. Karschnia P, Young JS, Dono A, Häni L, Sciortino T, Bruno F, Juenger ST, Teske N, Morshed RA, Haddad AF, et al. (2022). Prognostic validation of a new classification system for extent of resection in glioblastoma: a report of the RANO resect group. Neuro-Oncol. 10.1093/neuonc/noac193.
20. Gillis S, and Roth A (2020). PyClone-VI: scalable inference of clonal population structures using whole genome data. BMC Bioinformatics 21, 571. 10.1186/s12859-020-03919-2. [PubMed: 33302872]
21. Nathanson DA, Gini B, Mottahedeh J, Visnyei K, Koga T, Gomez G, Eskin A, Hwang K, Wang J, Masui K, et al. (2014). Targeted therapy resistance mediated by dynamic regulation of extrachromosomal mutant EGFR DNA. Science 343, 72–76. 10.1126/science.1241328. [PubMed: 24310612]
22. Morton AR, Dogan-Artun N, Faber ZJ, MacLeod G, Bartels CF, Piazza MS, Allan KC, Mack SC, Wang X, Gimple RC, et al. (2019). Functional Enhancers Shape Extrachromosomal Oncogene Amplifications. Cell 179, 1330–1341 13. 10.1016/j.cell.2019.10.039. [PubMed: 31761532]
23. Wu S, Turner KM, Nguyen N, Raviram R, Erb M, and Santini J (2019). Circular ecDNA promotes accessible chromatin and high oncogene expression. Nature, 1–24. 10.1038/s41586-019-1763-5.
24. Kim H, Nguyen N-P, Turner K, Wu S, Gujar AD, and Luebeck J (2020). Extrachromosomal DNA is associated with oncogene amplification and poor outcome across multiple cancers. Nat. Genet, 1–20. 10.1038/s41588-020-0678-2. [PubMed: 31911675]
25. Turner KM, Deshpande V, Beyter D, Koga T, Rusert J, Lee C, Li B, Arden K, Ren B, Nathanson DA, et al. (2017). Extrachromosomal oncogene amplification drives tumour evolution and genetic heterogeneity. Nature 543, 122–125. 10.1038/nature21356. [PubMed: 28178237]
26. Perry A, Miller CR, Gujrati M, Scheithauer BW, Zambrano SC, Jost SC, Raghavan R, Qian J, Cochran EJ, Huse JT, et al. (2009). Malignant gliomas with primitive neuroectodermal tumor-like components: a clinicopathologic and genetic study of 53 cases. Brain Pathol. Zurich Switz. 19, 81–90. 10.1111/j.1750-3639.2008.00167.x.
27. Suwala AK, Stichel D, Schrimpf D, Maas SLN, Sill M, Dohmen H, Banan R, Reinhardt A, Sievers P, Hinz F, et al. (2021). Glioblastomas with primitive neuronal component harbor a distinct methylation and copy-number profile with inactivation of TP53, PTEN, and RB1. Acta Neuropathol. (Berl.) 142, 179–189. 10.1007/s00401-021-02302-6. [PubMed: 33876327]
28. Wang S, Lee S, Chu C, Jain D, Kerpedjiev P, Nelson GM, Walsh JM, Alver BH, and Park PJ (2020). HiNT: a computational method for detecting copy number variations and translocations from Hi-C data. Genome Biol. 21, 73. 10.1186/s13059-020-01986-5. [PubMed: 32293513]
29. Wang X, Luan Y, and Yue F (2022). EagleC: A deep-learning framework for detecting a full range of structural variations from bulk and single-cell contact maps. Sci. Adv. 8. 10.1126/sciadv.abn9215.
30. Dixon JR, Xu J, Dileep V, Zhan Y, Song F, Le VT, Yardımcı GG, Chakraborty A, Bann DV, Wang Y, et al. (2018). Integrative detection and analysis of structural variation in cancer genomes. Nat. Genet. 50, 1388–1398. 10.1038/s41588-018-0195-8. [PubMed: 30202056]
31. Stephens PJ, Greenman CD, Fu B, Yang F, Bignell GR, Mudie LJ, Pleasance ED, Lau KW, Beare D, Stebbings LA, et al. (2011). Massive Genomic Rearrangement Acquired in a Single Catastrophic Event during Cancer Development. Cell 144, 27–40. 10.1016/j.cell.2010.11.055. [PubMed: 21215367]
32. Cortés-Ciriano I, Lee JJ-K, Xi R, Jain D, Jung YL, Yang L, Gordenin D, Klimczak LJ, Zhang C-Z, Pellman DS, et al. (2020). Comprehensive analysis of chromothripsis in 2,658 human cancers using whole-genome sequencing. Nat. Genet. 52, 331–341. 10.1038/s41588-019-0576-7. [PubMed: 32025003]
33. Kleinman CL, Gerges N, Papillon-Cavanagh S, Sin-Chan P, Pramatarova A, Quang D-AK, Adoue V, Busche S, Caron M, Djambazian H, et al. (2014). Fusion of TTYH1 with the C19MC microRNA cluster drives expression of a brain-specific DNMT3B isoform in the embryonal brain tumor ETMR. Nat. Genet. 46, 39–44. 10.1038/ng.2849. [PubMed: 24316981]
34. Carbonara C, Longa L, Grosso E, Borrone C, Garré MG, Brisigotti M, and Migone N (1994). 9q34 loss of heterozygosity in a tuberous sclerosis astrocytoma suggests a growth suppressor-like activity also for the TSC1 gene. Hum. Mol. Genet. 3, 1829–1832. 10.1093/hmg/3.10.1829. [PubMed: 7849708]

35. Frattini V, Trifonov V, Chan JM, Castano A, Lia M, Abate F, Keir ST, Ji AX, Zoppoli P, Niola F, et al. (2013). The integrated landscape of driver genomic alterations in glioblastoma. Nat. Genet. 45, 1141–1149. 10.1038/ng.2734. [PubMed: 23917401]
36. Singh D, Chan JM, Zoppoli P, Niola F, Sullivan R, Castano A, Liu EM, Reichel J, Porrati P, Pellegatta S, et al. (2012). Transforming fusions of FGFR and TACC genes in human glioblastoma. Science 337, 1231–1235. 10.1126/science.1220834. [PubMed: 22837387]
37. Keskin DB, Anandappa AJ, Sun J, Tirosh I, Mathewson ND, Li S, Oliveira G, Giobbie-Hurder A, Felt K, Gjini E, et al. (2019). Neoantigen vaccine generates intratumoral T cell responses in phase Ib glioblastoma trial. Nature 565, 234–239. 10.1038/s41586-018-0792-9. [PubMed: 30568305]
38. Rojas LA, Sethna Z, Soares KC, Olcese C, Pang N, Patterson E, Lihm J, Ceglia N, Guasp P, Chu A, et al. (2023). Personalized RNA neoantigen vaccines stimulate T cells in pancreatic cancer. Nature 618, 144–150. 10.1038/s41586-023-06063-y. [PubMed: 37165196]
39. Sarkizova S, Klaeger S, Le PM, Li LW, Oliveira G, Keshishian H, Hartigan CR, Zhang W, Braun DA, Ligon KL, et al. (2020). A large peptidome dataset improves HLA class I epitope prediction across most of the human population. Nat. Biotechnol. 38, 199–209. 10.1038/s41587-019-0322-9. [PubMed: 31844290]
40. O'Donnell TJ, Rubinsteyn A, and Laserson U (2020). MHCflurry 2.0: Improved Pan-Allele Prediction of MHC Class I-Presented Peptides by Incorporating Antigen Processing. Cell Syst. 11, 42–48 7. [PubMed: 32711842]
41. Kelley KW, Nakao-Inoue H, Molofsky AV, and Oldham MC (2018). Variation among intact tissue samples reveals the core transcriptional features of human CNS cell classes. Nat. Neurosci. 1–24. 10.1038/s41593-018-0216-z.
42. Venkatesh HS, Morishita W, Geraghty AC, Silverbush D, Gillespie SM, Arzt M, Tam LT, Espenel C, Ponnuswami A, Ni L, et al. (2019). Electrical and synaptic integration of glioma into neural circuits. Nature 573, 539–545. 10.1038/s41586-019-1563-y. [PubMed: 31534222]
43. Venkataramani V, Yang Y, Schubert MC, Reyhan E, Tetzlaff SK, Wißmann N, Botz M, Soyka SJ, Beretta CA, Pramatarov RL, et al. (2022). Glioblastoma hijacks neuronal mechanisms for brain invasion. Cell 185, 2899–2917 31. 10.1016/j.cell.2022.06.054. [PubMed: 35914528]
44. Venkataramani V, Tanev DI, Strahle C, Studier-Fischer A, Fankhauser L, Kessler T, Körber C, Kardorff M, Ratliff M, Xie R, et al. (2019). Glutamatergic synaptic input to glioma cells drives brain tumour progression. Nature 573, 532–538. 10.1038/s41586-019-1564-x. [PubMed: 31534219]
45. Stewart M, Lau P, Banks G, Bains RS, Castroflorio E, Oliver PL, Dixon CL, Kruer MC, Kullmann DM, Acevedo-Arozena A, et al. (2019). Loss of Frrs1l disrupts synaptic AMPA receptor function, and results in neurodevelopmental, motor, cognitive and electrographical abnormalities. Dis. Model. Mech, dmm.036806. 10.1242/dmm.036806.
46. Schwenk J, Boudkkazi S, Kocylowski MK, Brechet A, Zolles G, Bus T, Costa K, Kollewe A, Jordan J, Bank J, et al. (2019). An ER Assembly Line of AMPA-Receptors Controls Excitatory Neurotransmission and Its Plasticity. Neuron 104, 680–692.e9. 10.1016/j.neuron.2019.08.033. [PubMed: 31604597]
47. MacDonald JI, Kubu CJ, and Meakin SO (2004). Nesca, a novel adapter, translocates to the nuclear envelope and regulates neurotrophin-induced neurite outgrowth. J. Cell Biol. 164, 851–862. 10.1083/jcb.200309081. [PubMed: 15024033]
48. Zhong S, Zhang S, Fan X, Wu Q, Yan L, Dong J, Zhang H, Li L, Sun L, Pan N, et al. (2018). A single-cell RNA-seq survey of the developmental landscape of the human prefrontal cortex. Nature 555, 524–528. 10.1038/nature25980. [PubMed: 29539641]
49. Abdelfattah N, Kumar P, Wang C, Leu JS, Flynn WF, Gao R, Baskin DS, Pichumani K, Ijare OB, Wood SL, et al. (2022). Single-cell analysis of human glioma and immune cells identifies S100A4 as an immunotherapy target. Nat. Commun. 13, 767. 10.1038/s41467-022-28372-y. [PubMed: 35140215]
50. Payne KK, Mine JA, Biswas S, Chaurio RA, Perales-Puchalt A, Anadon CM, Costich TL, Harro CM, Walrath J, Ming Q, et al. (2020). BTN3A1 governs antitumor responses by coordinating αβ and γδ T cells. Science 369, 942–949. 10.1126/science.aay2767. [PubMed: 32820120]

51. Jandus C, Boligan KF, Chijioke O, Liu H, Dahlhaus M, Démoulins T, Schneider C, Wehrli M, Hunger RE, Baerlocher GM, et al. (2014). Interactions between Siglec-7/9 receptors and ligands influence NK cell-dependent tumor immunosurveillance. J. Clin. Invest. 124, 1810–1820. 10.1172/JCI65899. [PubMed: 24569453]
52. Feng Y, Duan T, Du Y, Jin S, Wang M, Cui J, and Wang RF (2017). LRRC25 Functions as an Inhibitor of NF-κB Signaling Pathway by Promoting p65/RelA for Autophagic Degradation. Sci. Rep. 7, 13448. 10.1038/s41598-017-12573-3. [PubMed: 29044191]
53. Du Y, Duan T, Feng Y, Liu Q, Lin M, Cui J, and Wang R (2018). LRRC25 inhibits type I IFN signaling by targeting ISG15-associated RIG-I for autophagic degradation. EMBO J. 37, 351–366. 10.15252/embj.201796781. [PubMed: 29288164]
54. Kim Y, Varn FS, Park SH, Yoon BW, Park HR, Lee C, Verhaak RGW, and Paek SH (2021). Perspective of mesenchymal transformation in glioblastoma. Acta Neuropathol. Commun. 9, 50. 10.1186/s40478-021-01151-4. [PubMed: 33762019]
55. Hara T, Chanoch-Myers R, Mathewson ND, Myskiw C, Atta L, Bussema L, Eichhorn SW, Greenwald AC, Kinker GS, Rodman C, et al. (2021). Interactions between cancer cells and immune cells drive transitions to mesenchymal-like states in glioblastoma. Cancer Cell 39, 779–792.e11. 10.1016/j.ccell.2021.05.002. [PubMed: 34087162]
56. Comba A, Faisal SM, Dunn PJ, Argento AE, Hollon TC, and Al-Holou WN (2022). Spatiotemporal analysis of glioma heterogeneity reveals COL1A1 as an actionable target to disrupt tumor progression. Nat. Commun. 13, 3606–3623. 10.1038/s41467-022-31340-1. [PubMed: 35750880]
57. Jain S, Rick JW, Joshi RS, Beniwal A, Spatz J, Gill S, Chang AC-C, Choudhary N, Nguyen AT, Sudhir S, et al. (2023). Single-cell RNA sequencing and spatial transcriptomics reveal cancer-associated fibroblasts in glioblastoma with protumoral effects. J. Clin. Invest. 133, e147087. 10.1172/JCI147087. [PubMed: 36856115]
58. Cakir B, Tanaka Y, Kiral FR, Xiang Y, Dagliyan O, Wang J, Lee M, Greaney AM, Yang WS, duBoulay C, et al. (2022). Expression of the transcription factor PU.1 induces the generation of microglia-like cells in human cortical organoids. Nat. Commun. 13, 430. 10.1038/s41467-022-28043-y. [PubMed: 35058453]
59. Nowakowski TJ, Bhaduri A, Pollen AA, Alvarado B, Mostajo-Radji MA, and Lullo E (2017). Spatiotemporal gene expression trajectories reveal developmental hierarchies of the human cortex. Science 358, 1318–1323. 10.1126/science.aap8809. [PubMed: 29217575]
60. Marquis C, Fonseca CL, Queen KA, Wood L, Vandal SE, Malaby HLH, Clayton JE, and Stumpff J (2021). Chromosomally unstable tumor cells specifically require KIF18A for proliferation. Nat. Commun. 12, 1213. 10.1038/s41467-021-21447-2. [PubMed: 33619254]
61. Tamayo NA, Bourbeau MP, Allen JR, Ashton KS, Chen JJ, Kaller MR, Nguyen TT, Nishimura N, Pettus LH, Walton M, et al. (2022). Targeting the Mitotic Kinesin KIF18A in Chromosomally Unstable Cancers: Hit Optimization Toward an In Vivo Chemical Probe. J. Med. Chem. 65, 4972–4990. 10.1021/acs.jmedchem.1c02030. [PubMed: 35286090]
62. Pollen AA, Nowakowski TJ, Chen J, Retallack H, Sandoval-Espinosa C, Nicholas CR, Shuga J, Liu SJ, Oldham MC, Diaz A, et al. (2015). Molecular identity of human outer radial glia during cortical development. Cell 163, 55–67. 10.1016/j.cell.2015.09.004. [PubMed: 26406371]
63. Huang W, Bhaduri A, Velmeshev D, Wang S, Wang L, Rottkamp CA, Alvarez-Buylla A, Rowitch DH, and Kriegstein AR (2020). Origins and Proliferative States of Human Oligodendrocyte Precursor Cells. Cell 182, 594–608 11. 10.1016/j.cell.2020.06.027. [PubMed: 32679030]
64. Dixon JR, Jung I, Selvaraj S, Shen Y, Antosiewicz-Bourget JE, and Lee AY (2015). Chromatin architecture reorganization during stem cell differentiation. Nature, 1–23. 10.1038/nature14222.
65. Bhaduri A, Lullo E, Jung D, Müller S, Crouch EE, Espinosa CS, Ozawa T, Alvarado B, Spatazza J, Cadwell CR, et al. (2020). Outer Radial Glia-like Cancer Stem Cells Contribute to Heterogeneity of Glioblastoma. Cell Stem Cell 26, 48–63 6. 10.1016/j.stem.2019.11.015. [PubMed: 31901251]
66. Fujikawa A, Sugawara H, Tanaka T, Matsumoto M, Kuboyama K, Suzuki R, Tanga N, Ogata A, Masumura M, and Noda M (2017). Targeting PTPRZ inhibits stem cell-like properties and tumorigenicity in glioblastoma cells. Sci. Rep. 7, 5609. 10.1038/s41598-017-05931-8. [PubMed: 28717188]

67. Shi Y, Ping Y-F, Zhou W, He Z-C, Chen C, Bian B-S-J, Zhang L, Chen L, Lan X, Zhang X-C, et al. (2017). Tumour-associated macrophages secrete pleiotrophin to promote PTPRZ1 signalling in glioblastoma stem cells for tumour growth. Nat. Commun. 8, 15080. 10.1038/ncomms15080. [PubMed: 28569747]
68. Pebworth MP, Ross J, Andrews M, Bhaduri A, and Kriegstein AR (2021). Human intermediate progenitor diversity during cortical development. Proc. Natl. Acad. Sci. U. S. A. 118, 2019415118. 10.1073/pnas.2019415118.
69. Lemeille S, Paschaki M, Baas D, Morlé L, Duteyrat J-L, Ait-Lounis A, Barras E, Soulavie F, Jerber J, Thomas J, et al. (2020). Interplay of RFX transcription factors 1, 2 and 3 in motile ciliogenesis. Nucleic Acids Res. 48, 9019–9036. 10.1093/nar/gkaa625. [PubMed: 32725242]
70. Pataskar A, Jung J, Smialowski P, Noack F, Calegari F, Straub T, and Tiwari VK (2016). NeuroD1 reprograms chromatin and transcription factor landscapes to induce the neuronal program. EMBO J. 35, 24–45. 10.15252/embj.201591206. [PubMed: 26516211]
71. Zhang K, Hocker JD, Miller M, Hou X, Chiou J, Poirion OB, Qiu Y, Li YE, Gaulton KJ, Wang A, et al. (2021). A single-cell atlas of chromatin accessibility in the human genome. Cell 184, 5985–6001 19. 10.1016/j.cell.2021.10.024. [PubMed: 34774128]
72. Stolt CC, Rehberg S, Ader M, Lommes P, Riethmacher D, Schachner M, Bartsch U, and Wegner M (2002). Terminal differentiation of myelin-forming oligodendrocytes depends on the transcription factor Sox10. Genes Dev. 16, 165–170. 10.1101/gad.215802. [PubMed: 11799060]
73. Glasgow SM, Zhu W, Stolt CC, Huang TW, Chen F, LoTurco JJ, Neul JL, Wegner M, Mohila C, and Deneen B (2014). Mutual antagonism between Sox10 and NFIA regulates diversification of glial lineages and glioma subtypes. Nat. Neurosci. 17, 1322–1329. 10.1038/nn.3790. [PubMed: 25151262]
74. Kang P, Lee HK, Glasgow SM, Finley M, Donti T, Gaber ZB, Graham BH, Foster AE, Novitch BG, Gronostajski RM, et al. (2012). Sox9 and NFIA coordinate a transcriptional regulatory cascade during the initiation of gliogenesis. Neuron 74, 79–94. 10.1016/j.neuron.2012.01.024. [PubMed: 22500632]
75. Gimple RC, Kidwell RL, Kim LJY, Sun T, Gromovsky AD, Wu Q, Wolf M, Lv D, Bhargava S, Jiang L, et al. (2019). Glioma Stem Cell-Specific Superenhancer Promotes Polyunsaturated Fatty-Acid Synthesis to Support EGFR Signaling. Cancer Discov. 9, 1248–1267. 10.1158/2159-8290.CD-19-0061. [PubMed: 31201181]
76. Rehfeld F, Maticzka D, Grosser S, Knauff P, Eravci M, Vida I, Backofen R, and Wulczyn FG (2018). The RNA-binding protein ARPP21 controls dendritic branching by functionally opposing the miRNA it hosts. Nat. Commun. 9, 1235. 10.1038/s41467-018-03681-3. [PubMed: 29581509]
77. Wang H, Song X, Huang Q, Xu T, Yun D, Wang Y, Hu L, Yan Y, Chen H, Lu D, et al. (2019). LGALS3 Promotes Treatment Resistance in Glioblastoma and Is Associated with Tumor Risk and Prognosis. Cancer Epidemiol. Biomark. Prev. Publ. Am. Assoc. Cancer Res. Cosponsored Am. Soc. Prev. Oncol. 28, 760–769. 10.1158/1055-9965.EPI-18-0638.
78. Tsai YT, Wu AC, Yang WB, Kao TJ, Chuang JY, Chang WC, and Hsu TI (2019). ANGPTL4 Induces TMZ Resistance of Glioblastoma by Promoting Cancer Stemness Enrichment via the EGFR/AKT/4E-BP1 Cascade. Int. J. Mol. Sci. 20, 5625. 10.3390/ijms20225625. [PubMed: 31717924]
79. Alcantara Llaguno SR, Xie X, and Parada LF (2016). Cell of Origin and Cancer Stem Cells in Tumor Suppressor Mouse Models of Glioblastoma. Cold Spring Harb. Symp. Quant. Biol. 81, 31–36. 10.1101/sqb.2016.81.030973. [PubMed: 27815542]
80. Holland EC, Li Y, Celestino J, Dai C, Schaefer L, Sawaya RA, and Fuller GN (2000). Astrocytes give rise to oligodendrogliomas and astrocytomas after gene transfer of polyoma virus middle T antigen in vivo. Am. J. Pathol. 157, 1031–1037. 10.1016/S0002-9440(10)64615-9. [PubMed: 10980141]
81. Ignatova TN, Kukekov VG, Laywell ED, Suslov ON, Vrionis FD, and Steindler DA (2002). Human cortical glial tumors contain neural stem-like cells expressing astroglial and neuronal markers in vitro. Glia 39, 193–206. 10.1002/glia.10094. [PubMed: 12203386]
82. Ilkhanizadeh S, Lau J, Huang M, Foster DJ, Wong R, Frantz A, Wang S, Weiss WA, and Persson AI (2014). Glial Progenitors as Targets for Transformation in Glioma. In Advances in Cancer Research (Elsevier), pp. 1–65. 10.1016/B978-0-12-800249-0.00001-9.

83. Lee J, Kotliarova S, Kotliarov Y, Li A, Su Q, Donin NM, Pastorino S, Purow BW, Christopher N, Zhang W, et al. (2006). Tumor stem cells derived from glioblastomas cultured in bFGF and EGF more closely mirror the phenotype and genotype of primary tumors than do serum-cultured cell lines. Cancer Cell 9, 391–403. 10.1016/j.ccr.2006.03.030. [PubMed: 16697959]
84. Sugiarto S, Persson AI, Munoz EG, Waldhuber M, Lamagna C, Andor N, Hanecker P, Ayers-Ringler J, Phillips J, Siu J, et al. (2011). Asymmetry-Defective Oligodendrocyte Progenitors Are Glioma Precursors. Cancer Cell 20, 328–340. 10.1016/j.ccr.2011.08.011. [PubMed: 21907924]
85. Nowakowski TJ, and Salama SR (2022). Cerebral Organoids as an Experimental Platform for Human Neurogenomics. Cells 11, 2803. 10.3390/cells11182803. [PubMed: 36139380]
86. Koga T, Chaim IA, Benitez JA, Markmiller S, Parisian AD, Hevner RF, Turner KM, Hessenauer FM, D'Antonio M, Nguyen ND, et al. (2020). Longitudinal assessment of tumor development using cancer avatars derived from genetically engineered pluripotent stem cells. Nat. Commun. 11, 550. 10.1038/s41467-020-14312-1. [PubMed: 31992716]
87. Han SJ, Morshed RA, Troncon I, Jordan KM, Henry RG, Hervey-Jumper SL, and Berger MS (2019). Subcortical stimulation mapping of descending motor pathways for perirolandic gliomas: assessment of morbidity and functional outcome in 702 cases. J. Neurosurg. 131, 201–208. 10.3171/2018.3.JNS172494.
88. Hervey-Jumper SL, Li J, Lau D, Molinaro AM, Perry DW, Meng L, and Berger MS (2015). Awake craniotomy to maximize glioma resection: methods and technical nuances over a 27-year period. J. Neurosurg. 123, 325–339. 10.3171/2014.10.JNS141520. [PubMed: 25909573]
89. Jenkinson M, and Smith S (2001). A global optimisation method for robust affine registration of brain images. Med Image Anal 5, 143–156. [PubMed: 11516708]
90. Jenkinson M, Bannister P, Brady M, and Smith S (2002). Improved optimization for the robust and accurate linear registration and motion correction of brain images. Neuroimage 17, 825–841. [PubMed: 12377157]
91. Smith SM (2002). Fast robust automated brain extraction. Hum Brain Mapp 17, 143–155. [PubMed: 12391568]
92. Fedorov A (3D). Slicer as an image computing platform for the Quantitative Imaging Network. Magn Reson Imaging 30, 1323–1341.
93. Kline CN, Joseph NM, Grenert JP, Van Ziffle J, Talevich E, Onodera C, Aboian M, Cha S, Raleigh DR, Braunstein S, et al. (2016). Targeted next-generation sequencing of pediatric neuro-oncology patients improves diagnosis, identifies pathogenic germline mutations, and directs targeted therapy. Neuro-Oncol, now254. 10.1093/neuonc/now254.
94. Johnson BE (2014). Mutational analysis reveals the origin and therapy-driven evolution of recurrent glioma. Science 343, 189–193. [PubMed: 24336570]
95. Paradis E and K. (2019). Schliep, ape 5.0: an environment for modern phylogenetics and evolutionary analyses in R. Bioinformatics 35, 526–528. [PubMed: 30016406]
96. Shen R, and Seshan VE (2016). FACETS: allele-specific copy number and clonal heterogeneity analysis tool for high-throughput DNA sequencing. Nucleic Acids Res 19;44(16):e131. 10.1093/nar/gkw520.
97. Li H, Handsaker B, Wysoker A, Fennell T, Ruan J, Homer N, Marth G, Abecasis G, Durbin R, and 1000 Genome Project Data Processing Subgroup (2009). The Sequence Alignment/Map format and SAMtools. Bioinformatics 25, 2078–2079. 10.1093/bioinformatics/btp352. [PubMed: 19505943]
98. Van Der Auwera GA, Carneiro MO, Hartl C, Poplin R, Del Angel G, Levy-Moonshine A, Jordan T, Shakir K, Roazen D, Thibault J, et al. (2013). From FastQ Data to High-Confidence Variant Calls: The Genome Analysis Toolkit Best Practices Pipeline. Curr. Protoc. Bioinforma 43. 10.1002/0471250953.bi1110s43.
99. Zaccaria S, and Raphael BJ (2020). Accurate quantification of copy-number aberrations and whole-genome duplications in multi-sample tumor sequencing data. Nat Commun 11, 4301. [PubMed: 32879317]
100. Dobin A (2013). STAR: ultrafast universal RNA-seq aligner. Bioinformatics 29, 15–21. [PubMed: 23104886]

101. Li B, and Dewey CN (2011). RSEM: accurate transcript quantification from RNA-Seq data with or without a reference genome. BMC Bioinformatics 12, 323. [PubMed: 21816040]
102. Corces MR, Granja JM, Shams S, Louie BH, Seoane JA, and Zhou W (2018). The chromatin accessibility landscape of primary human cancers. Science 362. 10.1126/science.aav1898.
103. Langmead B, and Salzberg SL (2012). Fast gapped-read alignment with Bowtie 2. Nat Methods 9, 357–359. [PubMed: 22388286]
104. Zhang Y (2008). Model-based analysis of ChIP-Seq (MACS. Genome Biol 9, 137.
105. Ramírez F, Ryan DP, Grüning B, Bhardwaj V, Kilpert F, Richter AS, Heyne S, Dündar F, and Manke T (2016). deepTools2: a next generation web server for deep-sequencing data analysis. Nucleic Acids Res. 44, W160–W165. 10.1093/nar/gkw257. [PubMed: 27079975]
106. Robinson MD, McCarthy DJ, and Smyth GK (2010). edgeR: a Bioconductor package for differential expression analysis of digital gene expression data. Bioinformatics 26, 139–140. [PubMed: 19910308]
107. Stuart T, Srivastava A, Madad S, Lareau CA, and Satija R (2021). Single-cell chromatin state analysis with Signac. Nat. Methods 18, 1333–1341. 10.1038/s41592-021-01282-5. [PubMed: 34725479]
108. Nikolic A, Singhal D, Ellestad K, Johnston M, Shen Y, Gillmor A, Morrissy S, Cairncross JG, Jones S, Lupien M, et al. (2021). Copy-scAT: Deconvoluting single-cell chromatin accessibility of genetic subclones in cancer. Sci. Adv. 7. 10.1126/sciadv.abg6045.
109. Schep AN, Wu B, Buenrostro JD, and Greenleaf WJ (2017). chromVAR: inferring transcription-factor-associated accessibility from single-cell epigenomic data. Nat. Methods 14, 975–978. 10.1038/nmeth.4401. [PubMed: 28825706]
110. Wang X (2016). runHiC: A user-friendly Hi-C data processing software based on hiclib. Zenodo. 10.5281/zenodo.55324.
111. Li H, and Durbin R (2009). Fast and accurate short read alignment with Burrows-Wheeler transform. Bioinformatics 25, 1754–1760. [PubMed: 19451168]
112. Durand NC (2016). Juicer Provides a One-Click System for Analyzing Loop-Resolution Hi-C Experiments. Cell Syst 3, 95–98. [PubMed: 27467249]
113. Salameh TJ, Wang X, Song F, Zhang B, Wright SM, Khunsriraksakul C, Ruan Y, and Yue F (2020). A supervised learning framework for chromatin loop detection in genome-wide contact maps. Nat Commun 11, 3428. [PubMed: 32647330]
114. Open2C, Nezar Abdennur, Sameer Abraham, Geoffrey Fudenberg, Flyamer Ilya M., Galitsyna Aleksandra A., Goloborodko Anton, Imakaev Maxim, Oksuz Betul A., and Venev Sergey V. (2022). Cooltools: enabling high-resolution Hi-C analysis in Python. bioRxiv, 2022.10.31.514564. 10.1101/2022.10.31.514564.
115. Wang X, Xu J, Zhang B, Hou Y, Song F, Lyu H, and Yue F (2021). Genome-wide detection of enhancer-hijacking events from chromatin interaction data in rearranged genomes. Nat Methods 18, 661–668. [PubMed: 34092790]
116. Uhrig S, Ellermann J, Walther T, Burkhardt P, Fröhlich M, and Hutter B (2021). Accurate and efficient detection of gene fusions from RNA sequencing data. Genome Res. 31, 448–460. 10.1101/gr.257246.119. [PubMed: 33441414]
117. Szolek A, Schubert B, Mohr C, Sturm M, Feldhahn M, and Kohlbacher O (2014). OptiType: Precision HLA Typing from next-Generation Sequencing Data. Bioinformatics 30, 3310–3316. [PubMed: 25143287]
118. O'Donnell TJ, Rubinsteyn A, Bonsack M, Riemer AB, Laserson U, and Hammerbacher J (2018). MHCflurry: Open-Source Class I MHC Binding Affinity Prediction. Cell Syst. 7, 129–132 4. 10.1016/j.cels.2018.05.014. [PubMed: 29960884]
119. Langfelder P, and Horvath S (2008). WGCNA: an R package for weighted correlation network analysis. BMC Bioinformatics 9, 559. [PubMed: 19114008]
120. Oldham MC, Horvath S, and Geschwind DH (2006). Conservation and evolution of gene coexpression networks in human and chimpanzee brains. Proc Natl Acad Sci USA 103, 17973–17978. [PubMed: 17101986]
121. Horvath S, and Dong J (2008). Geometric interpretation of gene coexpression network analysis. PLoS Comput Biol 4, 1000117.

122. Doncheva NT, Morris JH, Gorodkin J, and Jensen LJ (2019). Cytoscape StringApp: Network Analysis and Visualization of Proteomics Data. J Proteome Res 1;18(2):623–632. 10.1021/acs.jproteome.8b00702.

123. Heinz S, Benner C, Spann N, Bertolino E, Lin YC, Laslo P, Cheng JX, Murre C, Singh H, and Glass CK (2010). Simple combinations of lineage-determining transcription factors prime cis-regulatory elements required for macrophage and B cell identities. Mol Cell 38, 576–589. [PubMed: 20513432]

124. Li Z, Schulz MH, Look T, Begemann M, Zenke M, and Costa IG (2019). Identification of transcription factor binding sites using ATAC-seq. Genome Biol 20, 45. [PubMed: 30808370]

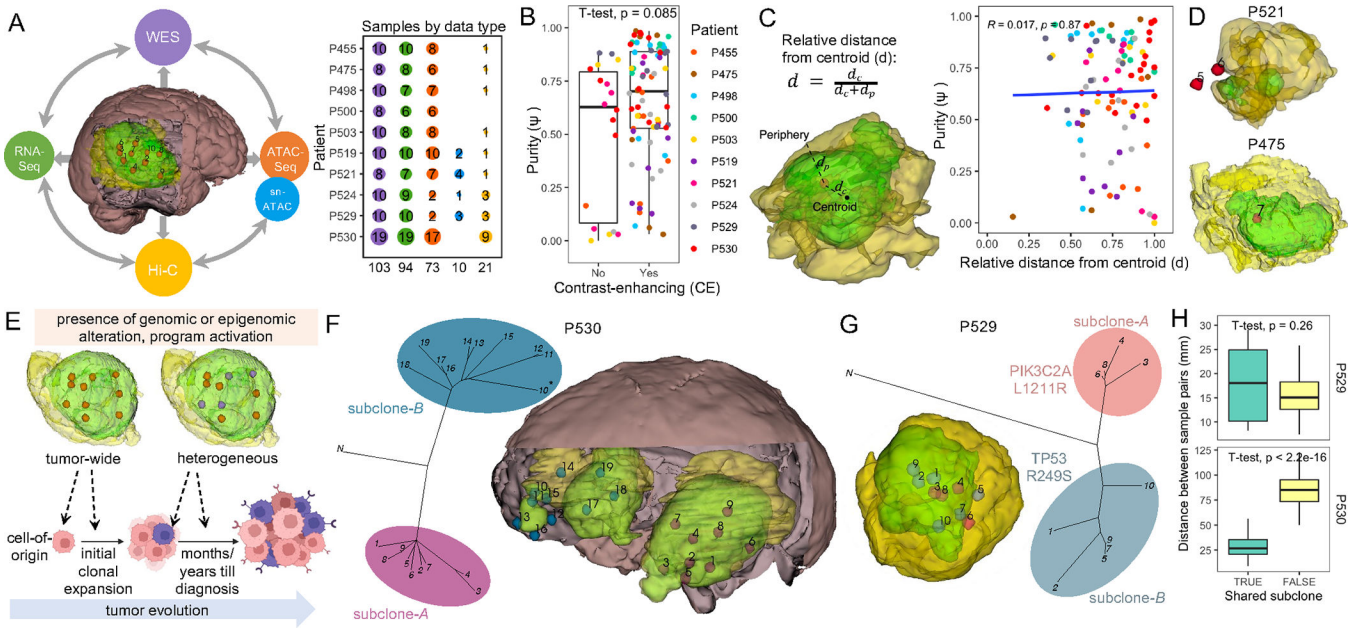

Figure 1: 3D spatial sampling reveals patterns of GBM infiltration and clonal expansion

A) 3D model shows sample locations in context of the whole-tumor (yellow) and contrast-enhancing lesion (green). The number of samples with high-quality whole-exome sequencing (WES), RNA-Seq, Hi-C, and tissue and/or single-nucleus (sn-) ATAC-Seq datasets is shown.

B) Purity (ψ) of samples located within (n=78) or outside (n=18) contrast-enhancing (CE) tumor regions, colored by patient.

C) Calculation of relative distance from centroid (*d*) using measurements of minimum sample distance to tumor centroid (d_C) and periphery (d_p) (left) and association with purity (ψ) (right, legend as in 1B).

D) 3D models showing low-purity samples P521_5, (ψ=0.03), P521_6 (ψ=0.06), and P457_7 (ψ=0.03).

E) Schematic illustrating inference of evolutionary trajectories by whole-tumor sampling.

F) Phylogenetic tree and 3D model for P530 show that samples 1–9 (subclone-*A*) are located in the temporal region and samples 10–19 (subclone-*B*) in the frontal region. Samples marked * have purity <0.5.

G) Phylogenetic tree and 3D model for P529 show that samples 3, 4, 6, 8 (subclone-*A*) and samples 1, 2, 5, 7, 9, and 10 (subclone-*B*) are spatially intermixed.

H) Distances between sample pairs (mm) from the same or different genetic subclone for P529 and P530.

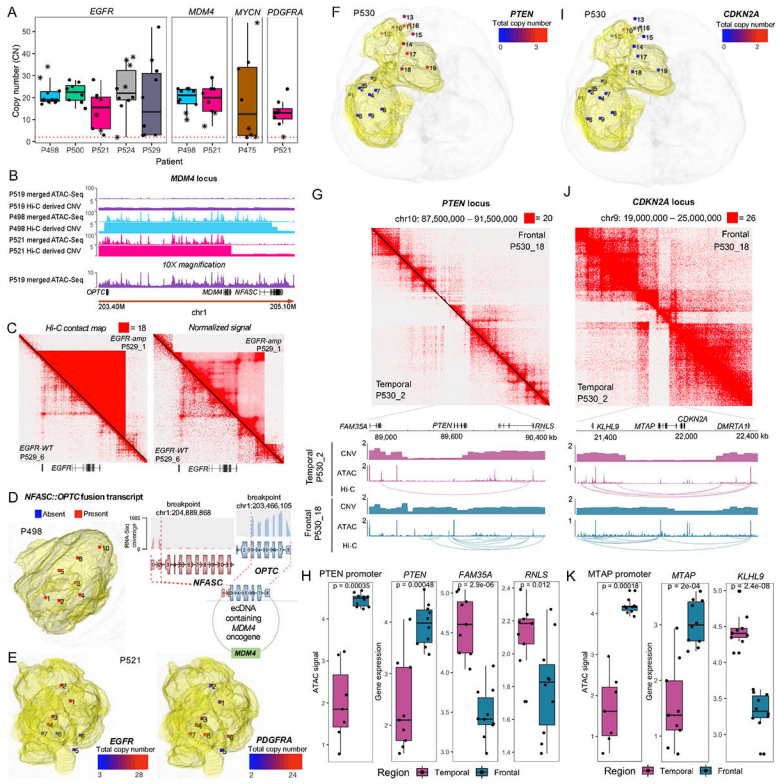

Figure 2: Oncogene amplification and tumor suppressor deletion on the whole-tumor scale.

A) WES-derived copy number (CN) for all amplifications detected across patients. Red dotted line indicates CN=2 (diploid). Samples marked * have purity <0.5.

B) ATAC-Seq and Hi-C-derived copy number variant (CNV) tracks in a patient without *MDM4* amplification (P519) and two patients with tumor-wide *MDM4* amplification (P498 and P521). The P519 ATAC-Seq track with 10X magnification is also shown.

C) Hi-C maps comparing samples with (P529_1, upper-right) and without (P529_6, lower-left) *EGFR* amplification. Map with normalized signal also shown.

D) 3D model showing tumor-wide *NFASC*::*OPTC* fusion transcript in P498. RNA-Seq track shows increased expression of *NFASC* and *OPTC* exons included in the fusion.

E) 3D models showing *EGFR* versus *PDGFRA* amplification in P521.

F) 3D model showing loss of *PTEN* in temporal region of P530.

G) Hi-C map at *PTEN* locus comparing representative samples from P530 frontal (P530_18, upper right) and temporal (P530_2, lower left) regions. CNV, ATAC-Seq, and Hi-C loop tracks are shown below.

H) ATAC signal at *PTEN* promoter and expression of *PTEN, FAM35A*, and *RNLS* in samples from the temporal versus frontal region. Statistical significance evaluated by T-tests.

I) 3D model shows loss of *CDKN2A* in all P530 samples except P530_10 (ψ=0.49).

J) Same as (G) for *CDKN2A* locus.

K) Same as (H) for *MTAP* promoter and *MTAP* and *KLHL9* expression.

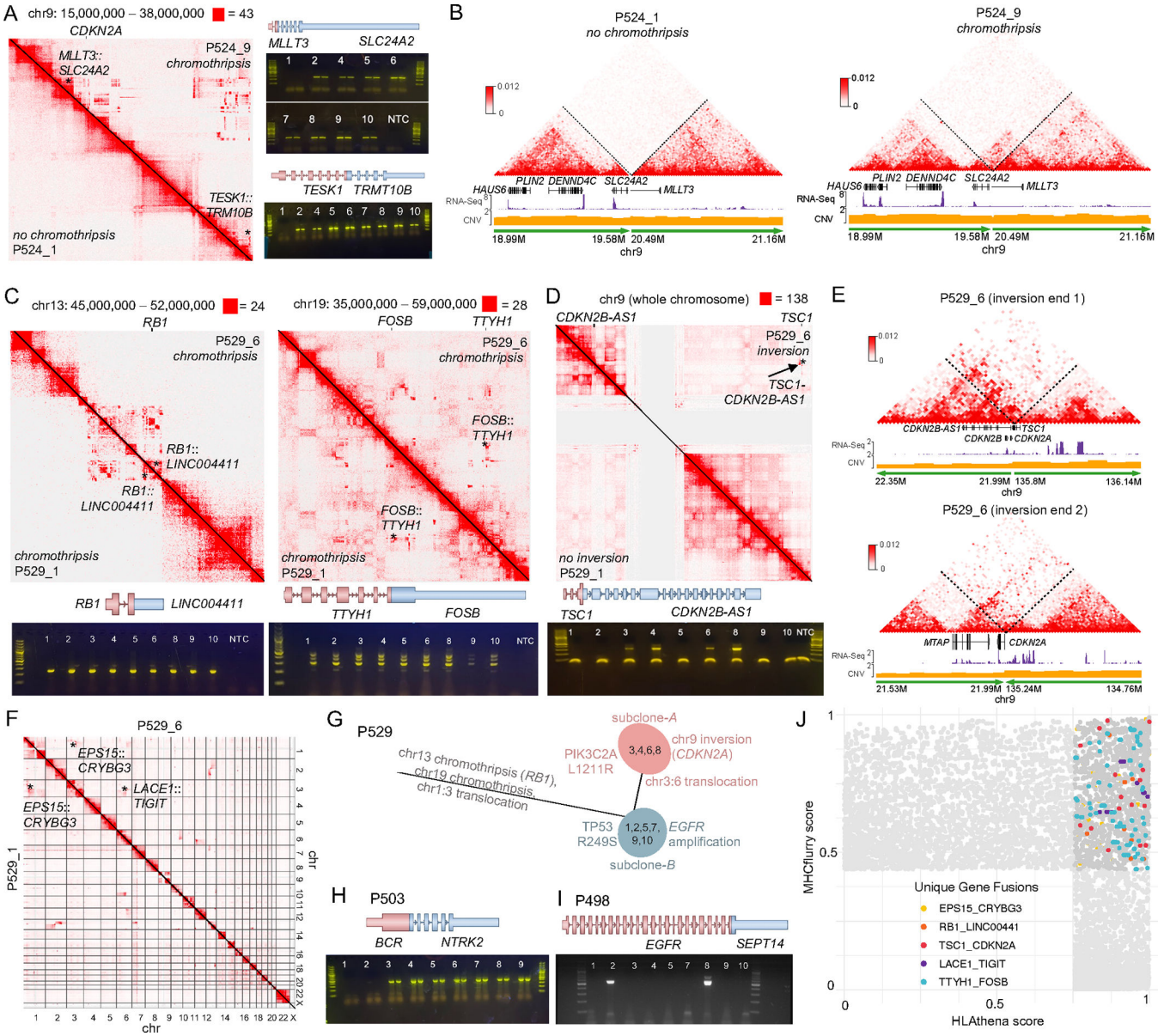

Figure 3: Structural variants massively disrupt the genome and epigenome at multiple stages of GBM evolution.

A) Hi-C maps show chromothripsis on chr9 in P524_9 (upper right, ψ=0.89), but not in low-purity sample P524_1 (lower left, ψ=0.04). RT-PCR and Sanger sequencing validate presence of *MLLT3*::*SLC24A2* and *TESK*::*TRMT10B* fusion transcripts in all samples except P524_1 (NTC=no template control).

B) Reconstruction of Hi-C maps at *MLLT3*::*SLC24A2* fusion junction reveals aberrant interactions across deletion breakpoints.

C) Hi-C maps show chromothripsis on chr13 (left) and chr19 (right) in P529_1 and P529_6. Fusion transcripts *RB1*::*LINC004411* and *TTYH1*::*FOSB* (bottom band) are present in all P529 samples.

D) Hi-C maps show chr9 inversion in P529_6 (arrow), but not in P529_1. *TSC1-CDKN2B-AS1* fusion transcript is present only in samples 3, 4, 6, 8 (upper band).
E) Reconstruction of Hi-C maps at both ends of chr9 inversion.
F) Inter-chromosomal Hi-C maps for P529_6 versus P529_1. The chr1:3 translocation creating the *EPS15*::*CRYBG3* fusion is present in both samples while the chr3:6 translocation creating the *LACE1*::*TIGIT* fusion is present only in P529_6.
G) Mutation-based phylogenetic tree for P529 (Fig 1G) labeled with additional tumor-wide and subclonal genomic alterations.
H) *BCR*::*NTRK2* fusion transcript detected in all P503 samples except those with low purity (P503_1 ψ=0.00, P503_2 ψ=0.03).
I) *EGFR-SEPT14* fusion transcript is detected only in two samples from P498.
J) MHC-I presentation predictions by MHCflurry and HLAthena for fusion-derived peptides in P529. Candidates passing both algorithms are highlighted for RT-PCR validated fusions.

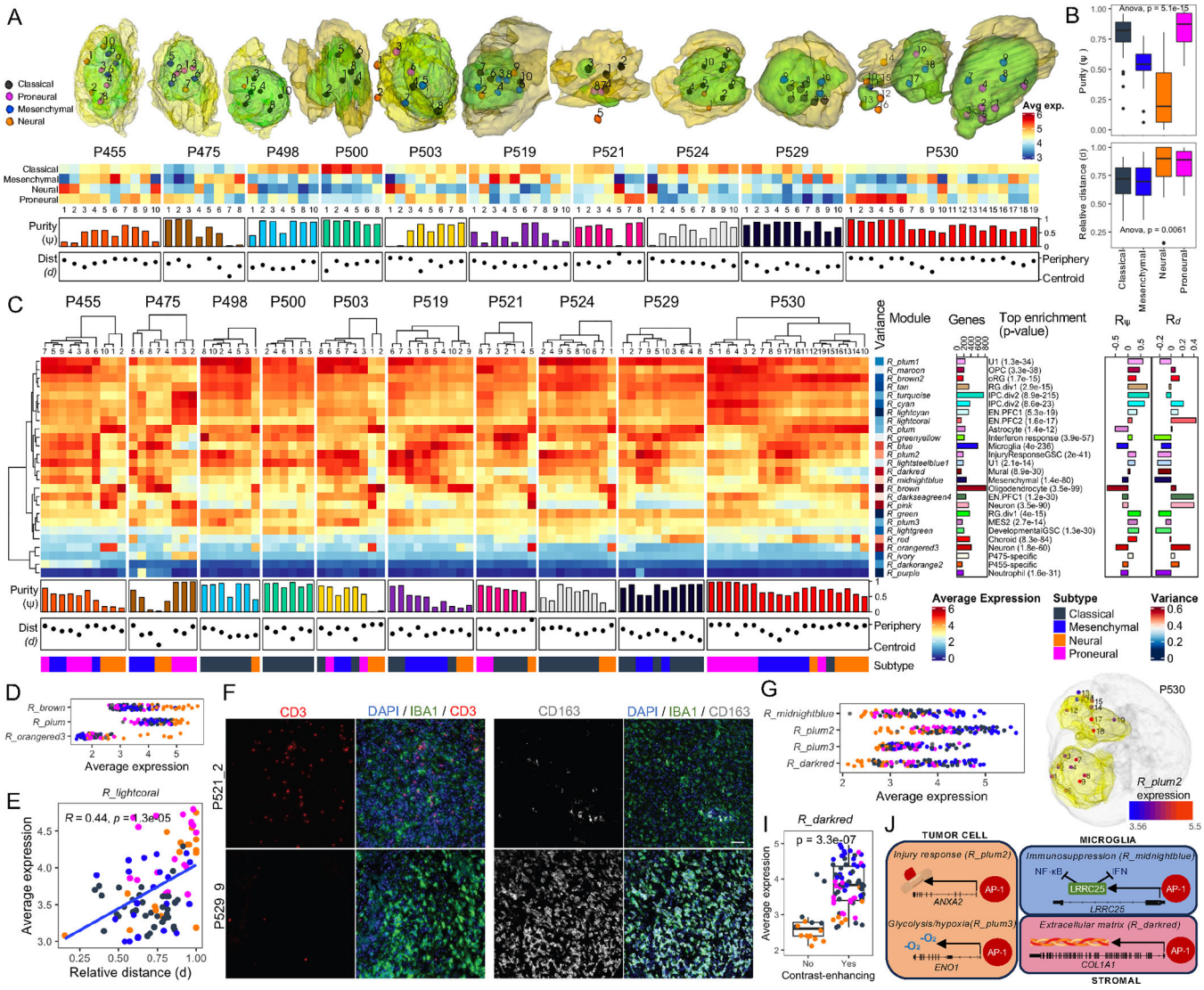

Figure 4: Transcriptomic heterogeneity in 3D spatially-defined GBM microenvironments.

A) 3D models show samples colored by subtype with highest average expression. Heatmap shows average expression for all subtypes with annotations for sample purity (ψ) and relative distance from centroid (*d*).

B) Purity (ψ, above) and relative distance from centroid (*d*, bottom) for samples classified by subtype.

C) Heatmap shows average expression of genes in each RNA module (*R_*) across samples annotated by purity (ψ), relative distance from centroid (*d*), and subtype. Variance across samples is shown for each module with annotations for number of constituent genes, top result from enrichment analysis, and correlations with sample purity (R_{ψ}) and relative distance from centroid (R_d).

D) Average expression of *R_brown* (oligodendrocyte), *R_plum* (astrocyte), and *R_orangered3* (neuron) modules across samples colored by subtype (legend as in 4C).

E) Average expression of *R_lightcoral* versus relative sample distance from centroid (*d*), colored by subtype.

F) Representative images of tumor targets from P521_2 and P529_9 with immunostaining for T cells (CD3, red), microglia/macrophages (Iba1, green), and a marker of immunosuppressive alternatively activated microglia/macrophages (CD163, white). Nuclei are stained with DAPI (blue) and bar denotes 50 um.

G) Average expression of *R_midnightblue, R_plum2, R_plum3,* and *R_darkred* across samples colored by subtype.

H) 3D model for P530 shows average expression of *R_plum2* across samples.

I) Average expression of *R_darkred* in samples from contrast-enhancing (CE) and non-CE regions, colored by subtype.

J) Summary figure showing AP-1-driven mesenchymal differentiation programs active in tumor cells, microglia, and stromal cells.

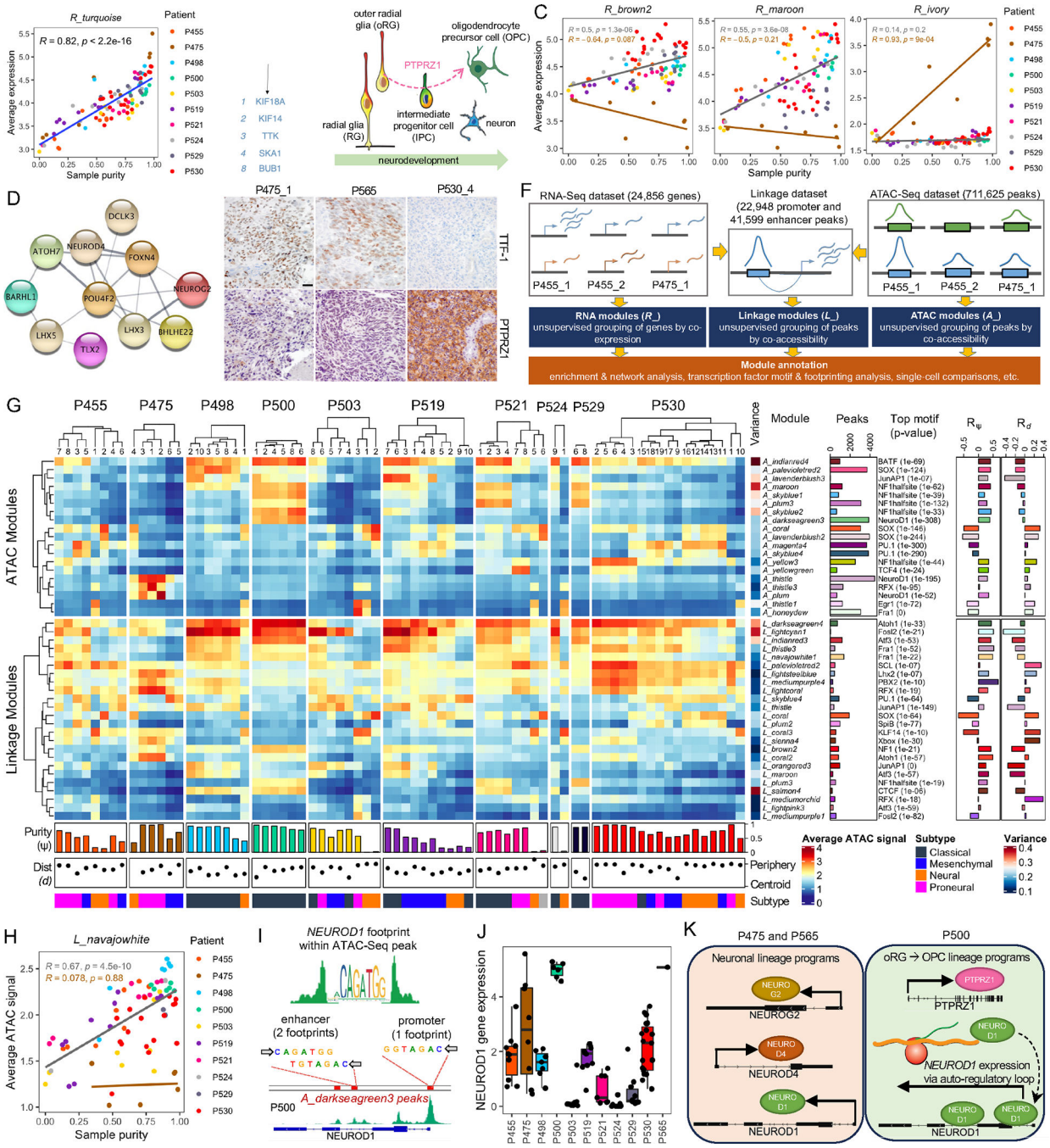

Figure 5: Neurodevelopmental programs reflect GBM lineage origins and contribute to heterogeneity.

A) Average expression of *R_turquoise* versus sample purity (ψ) colored by patient. Venn diagram shows overlap of *R_turquoise* constituent genes with the IPC.div2 signature; top-ranked genes within overlap are shown.

B) Schematic illustrating differentiation of radial glia (RG) and outer radial glia (oRG) through intermediate progenitor cells (IPCs) to oligodendrocyte precursor cells (OPCs) or neurons. *PTPRZ1* is expressed through oRG differentiation to OPCs.

C) Average expression of *R_brown2, R_maroon,* and *R_ivory* by sample purity (ψ) colored by patient. Linear model shown separately for P475 (brown) and remaining 9 patients (grey).
D) Drivers of neuronal fate specification identified by STRING network analysis of *R_ivory* constituent genes.
E) Immunohistochemical staining for TTF-1 and PTPRZ1 protein in representative tumor tissue sections from two patients with IDH-WT GBM with primitive neuronal component (P475 and P565) and one without (P530). Bar denotes 30μm.
F) Schematic showing derivation and annotation of RNA (*R_*), Linkage (*L_*), and ATAC (*A_*) modules from transcriptomic and chromatin landscape datasets.
G) Heatmap showing average ATAC-Seq signal for ATAC (*A_*) and linkage (*L_*) modules across samples annotated by purity (ψ), relative distance from centroid (*d*), and subtype. Variance across samples is shown for all modules annotated by number of constituent peaks, top result from motif analysis, and correlations with sample purity (R_{ψ}) and relative distance from centroid (R_d).
H) Average ATAC signal for *L_navajowhite1* by sample purity (ψ) colored by patient. Linear model shown separately for P475 (brown) and remaining patients (grey).
I) Transcription factor footprinting identifies NEUROD1 binding sites within *A_darkseagreen3* peaks at the *NEUROD1* promoter and an intronic *NEUROD1* enhancer. Merged ATAC-Seq track for P500 samples is shown.
J) *NEUROD1* gene expression for samples from all patients including P565.
K) Summary of distinct mechanisms of NEUROD1 activation in GBM from the common lineage origin (P500) versus GBM with primitive neuronal component (P475 and P565).

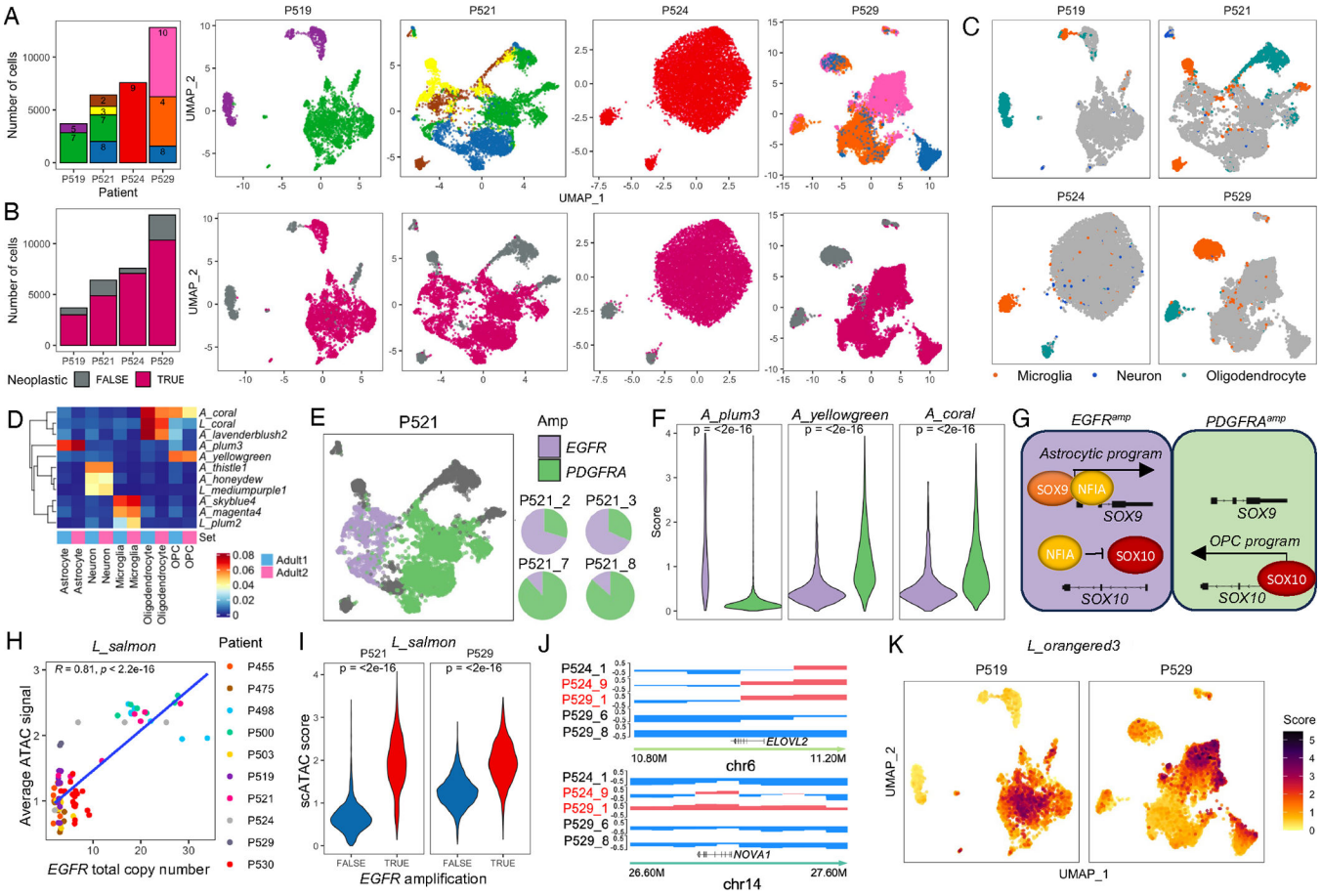

Figure 6: Intratumoral heterogeneity of GBM chromatin landscapes from 3D-spatial to single-cell resolution

A) Number of cells profiled by snATAC with UMAP projections, colored by sample.

B) Same as (A) colored by neoplastic status.

C) Cells with highest read-in-peak scores for modules associated with microglia (*A_magenta4, A_skyblue4, L_plum2*), neurons (*A_thistle1; A_honeydew, L_mediumpurple1*), or oligodendrocytes (*A_lavenderblush2; L_coral, A_coral*).

D) Read-in-peak scores in cell types from normal adult brain.

E) *EGFR* versus *PDGFRA*-amplified cells from P521. Proportion of *EGFR* v. *PDGFRA* amplified neoplastic cells also shown for individual samples.

F) Read-in-peak scores for *A_plum3, A_yellowgreen,* and *A_coral* in *EGFR*-amplified versus *PDGFRA*-amplified neoplastic cells from P521. Legend as in (E).

G) Summary figure showing NFIA/SOX9-mediated activation of the astrocytic program and SOX10-mediated activation of the OPC program in *EGFR* versus *PDGFRA*-amplified cells from P521.

H) Average ATAC signal of *L_salmon4* versus *EGFR* copy number, colored by patient.

I) Read-in-peak scores for *L_salmon4* in neoplastic cells with and without *EGFR* amplification from P521 and P529.

J) Hi-C-derived A/B tracks showing *ELOVL2* and *NOVA1* in open ‘A’ chromatin compartments only in *EGFR*-amplified samples P524_9 and P529_1.

K) Read-in-peak scores for *L_orangered3* in P519 and P529.

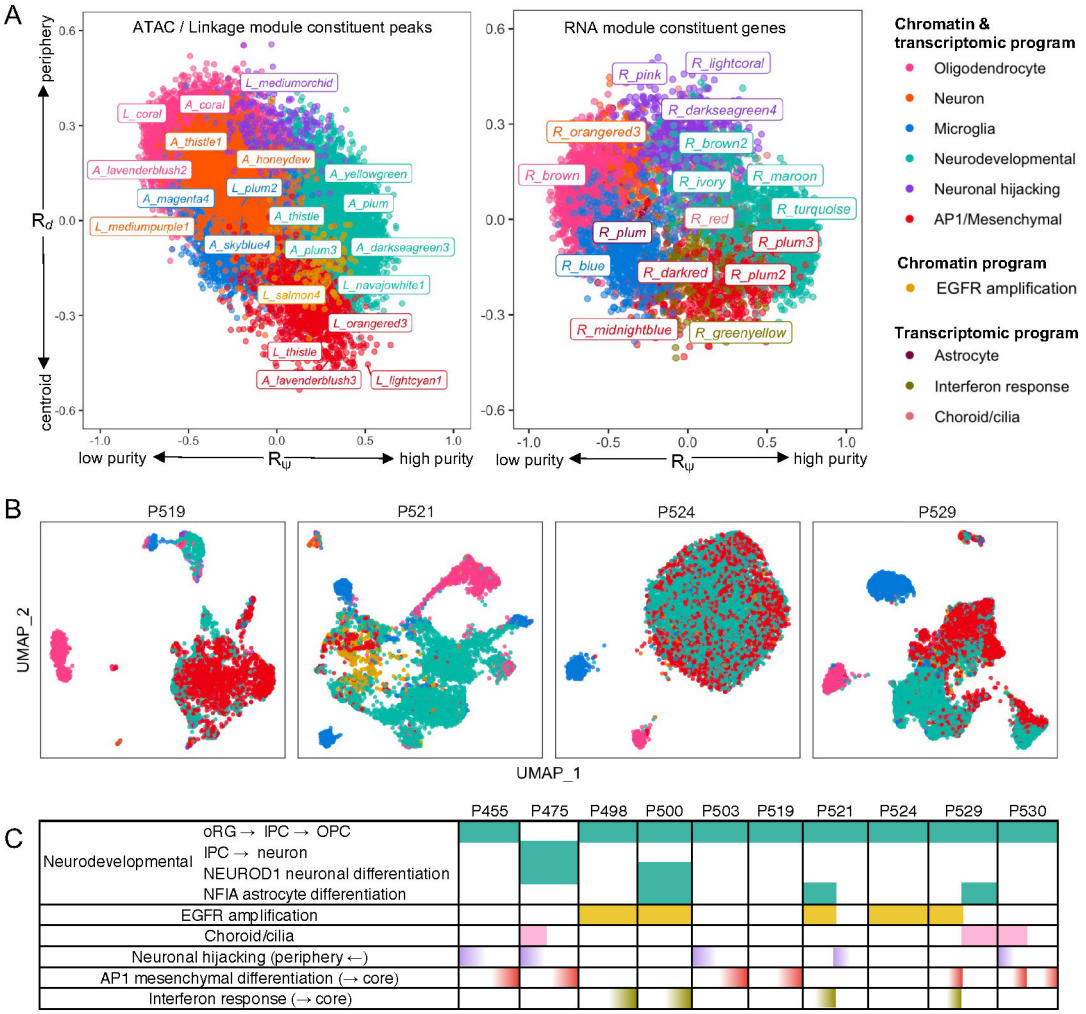

Figure 7: GBM heterogeneity and evolution redefined in 3D whole-tumor space.

A) GBM chromatin and transcriptomic programs in 3D whole-tumor space. Correlations with sample purity (R_ψ) and relative sample distance from centroid (R_d) are shown for individual constituent peaks of chromatin programs (left) and individual constituent genes of transcriptomic programs (right).

B) GBM chromatin programs at single-cell resolution. Cells are colored by chromatin program as in (A) for the module with most reads-in-peaks.

C) Summary table showing modular activation of GBM chromatin and gene expression programs in individual patients and tumor regions.

KEY RESOURCES TABLE

REAGENT or RESOURCE	SOURCE	IDENTIFIER
Antibodies		
CD163	Leica Biosystems, USA	Catalog # CD163-L-CE, mouse clone 10D6
IBA1	Wako Chemicals USA	Catalog#019–19741, polyclonal rabbit
CD204	Cosmo Bio USA	# KMU-MA01, clone SRA-E5
CD3	Leica Biosystems	Catalog #NCL-L-CD3– 565, clone LN10
PTPRZ1	BD Biosciences	Catalog #610179
Critical Commercial Assays		
Multimer HRP kit	Ventana Medical Systems, Inc., USA	
AllPrep DNA/RNA/ miRNA Universal Kit	QIAGEN	Cat.80224
KAPA Stranded mRNA-Seq Kit	Kapa Biosystems	KR0960-v2.14
Tagment DNA TDE1 Enzyme and Buffer Kits	Illumina	NX#-TD, NX#-TDE1
Chromium NextGEM Single Cell ATAC Kit v2	10X Genomics	N/A
iScript cDNA Synthesis Kit	BioRad	#1708891
Deposited Data		
Deposition of exome, RNA-Seq, ATAC-Seq, and Hi-C datasets	European Genome-Phenome Archive (EGA)	EGAS00001006785, EGAD00001005221/2, and EGAD00001009496/7
Deposition of processed single-cell ATAC-Seq datasets	GEO	GSE226726
Published GBM single-cell RNA-Seq dataset	Neftel, C. *et al.* An Integrative Model of Cellular States. *Plast. Genet. Glioblastoma Cell* 1–37 (2019) doi:10.1016/j.cell.2019.06.024.	GSE131928
Published GBM single-cell RNA-Seq dataset	Abdelfattah, N. *et al.* Single-cell analysis of human glioma and immune cells identifies S100A4 as an immunotherapy target. *Nat. Commun.* **13**, 767 (2022).	GSE182109
Published adult brain single-cell ATAC dataset	Zhang, K. *et al.* A single-cell atlas of chromatin accessibility in the human genome. *Cell***184**, 5985–6001 19 (2021).	N/A
Published fetal brain single-cell RNA-Seq dataset	Nowakowski, T. J. *et al.* Spatiotemporal gene expression trajectories reveal developmental hierarchies of the human cortex. *Science***358**, 1318–1323 (2017).	N/A
Published TCGA dataset	Ceccarelli, M. *et al.* Molecular Profiling Reveals Biologically Discrete Subsets and Pathways of Progression in Diffuse Glioma. *Cell***164**, 550–563 (2016).	N/A
Oligonucleotides		
Primers for fusion gene validation	See Table S4	N/A
Software and Algorithms		
Original R code	All original R code has been deposited at https://github.com/radhikamathur/3DSpatiallvMappedGBMs and is publicly available as of the date of publication.	N/A

REAGENT or RESOURCE	SOURCE	IDENTIFIER
Brainlab Cranial Navigation	BrainLAB AG	v3
3D Slicer	Fedorov, A. Slicer as an image computing platform for the Quantitative Imaging Network. *Magn Reson Imaging***30**, 1323–1341 (3D).	N/A
FACETS	Shen, R. & Seshan, V. E. FACETS: allele-specific copy number and clonal heterogeneity analysis tool for high- throughput DNA sequencing. *Nucleic Acids Res***19;44(16):e131**, (2016).	N/A
PyClone VI	Gillis, S. & Roth, A. PyClone-VI: scalable inference of clonal population structures using whole genome data. *BMC Bioinformatics***21**, 571 (2020).	v0.1.0
HATCHet	Zaccaria, S. & Raphael, B. J. Accurate quantification of copy-number aberrations and whole-genome duplications in multi-sample tumor sequencing data. *Nat Commun***11**, 4301 (2020).	v0.4.14
Bowtie2	Langmead, B. & Salzberg, S. L. Fast gapped-read alignment with Bowtie 2. *Nat Methods***9**, 357–9 (2012).	N/A
MACS2	Zhang, Y. Model-based analysis of ChIP-Seq (MACS. *Genome Biol***9**, 137 (2008).	N/A
Peakachu	Salameh, T. J. *et al.* A supervised learning framework for chromatin loop detection in genome-wide contact maps. *Nat Commun***11**, 3428 (2020).	N/A
EagleC	Wang, X., Luan, Y. & Yue, F. EagleC: A deep-learning framework for detecting a full range of structural variations from bulk and single-cell contact maps. *Sci. Adv.***8**, (2022).	N/A
NeoLoopFinder	Wang, X. *et al.* Genome-wide detection of enhancer-hijacking events from chromatin interaction data in rearranged genomes. *Nat Methods***18**, 661–668 (2021).	N/A
Arriba	Uhrig, S. *et al.* Accurate and efficient detection of gene fusions from RNA sequencing data. *Genome Res.* **31**, 448–460 (2021).	N/A
OptiType	Szolek, A. *et al.* OptiType: Precision HLA Typing from next- Generation Sequencing Data. *Bioinformatics***30**, 3310–16 (2014).	N/A
HLAthena	Sarkizova, S. *et al.* A large peptidome dataset improves HLA class I epitope prediction across most of the human population. *Nat. Biotechnol.* **38**, 199–209 (2020).	N/A
MHCFlurry 2.0	O'Donnell, T. J. *et al.* MHCflurry: Open-Source Class I MHC Binding Affinity Prediction. *Cell Syst.***7**, 129–132 4 (2018).	N/A
Cytoscape	Doncheva, N. T., Morris, J. H., Gorodkin, J. & Jensen, L. J. Cytoscape StringApp: Network Analysis and Visualization of Proteomics Data. *J Proteome Res***1;18(2):623–632**, (2019).	version3.9.1
STAR	Dobin, A. STAR: ultrafast universal RNA-seq aligner. *Bioinformatics***29**, 15–21 (2013).	N/A
RSEM	Li, B. & Dewey, C. N. RSEM: accurate transcript quantification from RNA-Seq data with or without a reference genome. *BMC Bioinformatics***12**, 323 (2011).	N/A
Copy-scATAC	Nikolic, A. *et al.* Copy-scAT: Deconvoluting single-cell chromatin accessibility of genetic subclones in cancer. *Sci. Adv.***7**, (2021).	N/A
Juicer	Durand, N. C. Juicer Provides a One-Click System for Analyzing Loop-Resolution Hi-C Experiments. *Cell Syst***3**, 95–8 (2016).	N/A